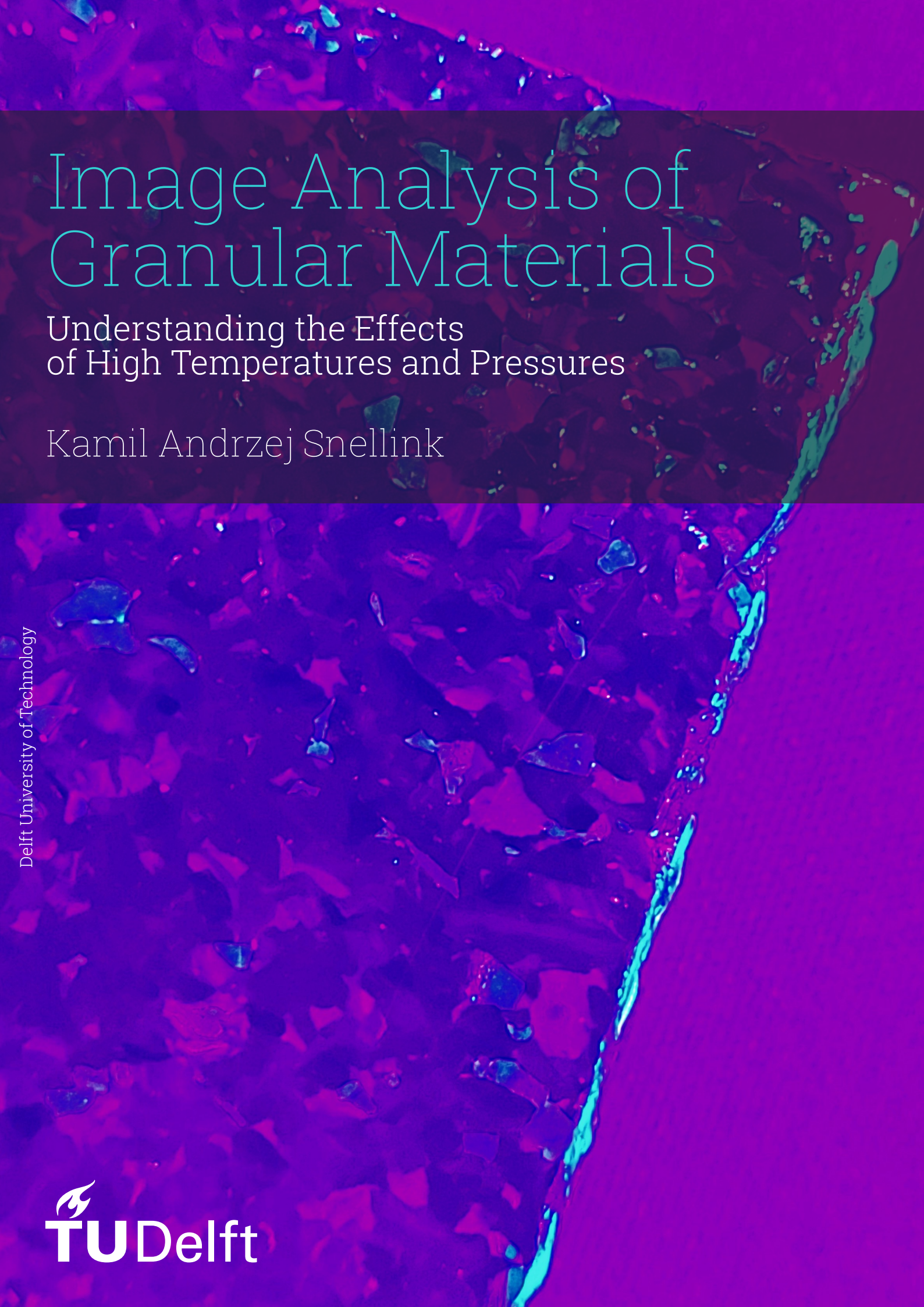

# Image Analysis of Granular Materials

## Understanding the Effects of High Temperatures and Pressures

Kamil Andrzej Snellink

Delft University of Technology

TU Delft

# Image Analysis of Granular Materials

## Understanding the Effects of High Temperatures and Pressures

by

Kamil Andrzej Snellink

to obtain the degree of Master of Science

at the Delft University of Technology,

to be defended publicly on Thursday the $17^{th}$ of July 2025 at 11 AM.


| | | | |
|---|---|---|---|
| Student number: | 5381886 | | |
| Project duration: | November, 2024 – July, 2025 | | |
| Thesis committee: | Dr. A. Barnhoorn | TU Delft | Supervisor |
| | Dr. T. Schmiedel | TU Delft | Supervisor |
| | Dr. ir. D.J.M Ngan-Tillard | TU Delft | Committee Member |

An electronic version of this thesis is available at `http://repository.tudelft.nl/`.


TU Delft

*Give me a rock, then I give you the numbers.*
- Karl-Heinz A.A. Wolf

**In memoriam**

# Preface

The topic for this thesis came forth on an October morning, while sitting in the mv room (from the study association *Mijnbouwkundige Vereeniging*). Professor Karl-Heinz Wolf walked in, we started a conversation and I remember him asking me, "will I see you for a subject this year?" I replied that it's the final year of my Master's, so I wouldn't see him anymore, "unless you have a thesis topic for me", I added. Indeed, he did have a topic, which resulted in the thesis you are reading right now. He helped me set up the thesis preparation, familiarised me with the samples and we had weekly meetings discussing not only the thesis, but also the study programme, developments in the energy industry and all kinds of other topics. It is therefore with great sadness that I received the horrible news of his illness; "plans need to be changed" is how he titled the e-mail in which he notified me about it. He made sure to hand me over to my new supervisors and, despite his worsening condition, he wanted to make sure that it would all work out. Sadly, he passed away long before the end of my thesis. I would like to express my gratitude to him with one simple word: **bedankt.**

The continuation of the thesis was made possible by Auke Barnhoorn, who was first supposed to be my second supervisor, and Tobias Schmiedel, who was able to join in on the project as well. I would like to take this opportunity to thank them both; even though it was not their topic and they were very busy, they were able to guide me further with comments, suggestions and help me whenever I got stuck somewhere. Furthermore, I would like to thank the lab team, especially Joost van Meel, who provided me with a nice spot in the lab, helped me build the image analysis setup and performed the CT scans. I also want to thank Dominique Ngan-Tillard for being my third supervisor during the defence. Last but not least, I would like to thank my classmates and other fellow students for carrying the rock samples to the lab, providing their view on the thesis whenever I asked them and of course for keeping me company on campus.

**Glück Auf!**

*Kamil Andrzej Snellink*
*'s Gravenhage, July 2025*

# Abstract

Understanding the behaviour of rocks subjected to high temperatures and pressures is essential for a wide range of subsurface applications. This thesis aims to develop an image analysis methodology to measure the porosities and permeabilities of rock samples. These samples were created as part of the doctoral thesis of K.H.A.A. Wolf by compacting rock rubble in a copper tube and subjecting it to various high temperatures and pressures. Despite earlier image analysis on these samples, there was an opportunity for improvement using higher-resolution imaging and more advanced processing techniques. Using a DSLR camera and 2 types of light (normal and UV), 33 samples were photographed and then analysed using Adobe Photoshop and ImageJ. Additionally, three samples were selected to be scanned using a $\mu CT$ scanner. The image processing included the conversion to greyscale, binarisation and the use of the morphological "open" operation. Porosity was directly measured, while permeability was estimated using a modified Kozeny-Carman equation. The quality of the impregnation of the sample with UV dye differed, yet for 28 out of the 33 samples, imaging with UV light worked better than with normal light. Using temperature data from when the samples were formed, a clear trend emerged showing that the higher the temperature, the lower the porosity and permeability become. This trend was also visible in the work by Wolf (2006) and the values were generally in agreement, except for the samples with extremely low porosities and permeabilities. While CT and image analysis gave similar porosity values, permeability results differed, highlighting the need for simulation-based permeability estimates from CT data. Further research into impregnation techniques is also recommended to enhance future image analysis workflows.

# Contents

# List of Figures

# List of Tables

# 1 Introduction

Porosity and permeability are among the most important properties for many subsurface applications. They are the determining factors when working with reservoirs. The effective porosity determines how much fluid can be stored in it, which gives an indication of the total hydrocarbon reserves in place (Alberts, 2005) or the quantity of hydrogen that can be stored. The variations in permeability (heterogeneities) are crucial in determining the amount of recoverable reserves, as they enhance or obstruct flow in different parts of a reservoir (Panda and Lake, 1994). Geothermal systems also depend on permeability for the transport of heat, significantly impacting production and injection capacities (Aqui and Zarrouk, 2011). Apart from reservoirs, porosity and permeability also play a role in many civil engineering applications such as groundwater management, foundation design and tunnel construction. Knowledge of these two factors is essential to ensure safe and durable infrastructure development (Šperl and Trčková, 2008).

There are also natural events in which porosity and permeability play a role. One of these is underground coal fires: events in which a coal seam is burning underground and sometimes at outcrops aboveground as well (Belcher, 2013). This not only causes environmental harm due to the emission of greenhouse gases and pollution of nearby water sources, but it can also pose a serious hazard to humans due to the initiation of forest fires or the creation of sinkholes (OSREM, 2025). Predicting the behaviour and spread of underground coal fires would allow people close to them to be notified and evacuated in time. The aim of the doctoral thesis by Wolf (2006) was therefore to model the fires. He made use of the work by Hettema (1996), who looked at underground coal gasification (UCG), a method that converts coal into gas using high temperatures, while it remains underground. Both in the case of natural coal fires and UCG, high temperatures and pressures caused by the fires lead to texture changes in the neighbouring sedimentary rocks, affecting their porosity and permeability.

Wolf (2006) performed 63 experiments in which rock rubble was put into a copper tube and subjected to temperatures of up to 1150 °C and pressures of up to 11 MPa. The aim was to simulate the conditions in different locations near the underground coal fires. These samples, as well as most of the experimental data, were preserved at the Faculty of Civil Engineering and Geosciences at the Delft University of Technology. As part of the research, image analysis was conducted on 33 of the samples to determine their porosity and permeability. These samples will be analysed again in this thesis, using modern imaging equipment with an increased spatial resolution as well as micro-CT scanning, to get a 3D view of the samples.

Image analysis is a technique that can be used to obtain information or extract useful features from an image (Russ, 1986). The process involves many steps, which need to be properly implemented to obtain the correct results. For digital image analysis, these include the capturing and storage of an image, correction of defects, segmentation of the objects of interest, binary image modification and measurement (Oberholzer et al., 1996). The advantage of image analysis over other techniques is the accessibility, cost and ease of use. To capture an image, all that is needed is a camera and the processing of the image can be done in open-source software like ImageJ (Schindelin et al., 2012). Other porosity measurement methods, such as the Washburn-Bunting method or the Boyle's law method, require laboratory setups (ScienceDi-

rect, n.d.). The drawback of image analysis is that it is a 2-dimensional measurement, while the rocks are 3-dimensional. This problem is amplified when measuring permeability, as it cannot be directly measured in 2D; rather, a formula has to be used to estimate it (Šperl and Trčková, 2008).

Image analysis has been used before to estimate the porosity of rock samples, like by Datta et al. (2015). They analysed thin sections of various types of rocks, concluding that the image analysis results comply with values from other sources. The report also emphasises the importance of image resolution to capture smaller pores and the fact that the thresholding technique has a significant influence on the porosity measure. Both of these will be explored in this report as well.

The effect of temperature/pressure on rocks has been studied extensively, although usually for lower temperatures, as these are more relevant in the context of hydrocarbon and geothermal reservoirs (Hassanzadegan et al., 2014; Jaber et al., 2024). The paper by Zhang et al. (2021) looked at the effect of temperatures between 25 and 1300 °C on the porosity of red sandstone using nuclear magnetic resonance. They found that below 500 °C there is no significant impact on the porosity, between 500 and 1000 °C the porosity and permeability increase due to the formation of cracks and above 1000 °C many of the minerals that compose the rocks melt, filling the pores and therefore decreasing the porosity. A study by G. Wu et al. (2013) meanwhile found an impact on the mechanical properties of sandstone around a temperature of 800 °C.

## 1.1. Aim of the Research

The motivation of this project is to revisit the experimental sample results with modern techniques: higher-resolution image analysis and CT scanning. The goal is to achieve a deeper understanding of the texture changes in compacted granular materials and to develop a methodology for image processing. The following four sub-questions will be answered:

- How does lighting affect photography for image analysis and how can it be optimised?
- What is the relation between high (bi-axial) stress/temperature and the porosity/permeability?
- How do the calculated porosities and permeabilities compare to those found by Wolf (2006) in terms of their absolute values and trends?
- Are the outcomes of the 2D image analysis similar to those of the 3D CT scanning?

Answering these questions will provide a modern insight into how image analysis can be used to quantify rocks, as well as the validation of previous work done by K.H.A.A. Wolf. This approach can be used not only for underground coal fires and their roof rocks but also for a range of other subsurface projects, as they often involve rock compaction due to high pressures and temperatures.

In the following section, the experiments performed by K.H.A.A. Wolf (2006) will be summarised. This is followed by a methodology chapter, describing the photography and CT-scanning setups, as well as the image analysis process. Thereafter, the results will be presented using graphs and images for clarity. Following this, in the discussion, the outcomes will be validated and recommendations for future research will be presented.

## 1.2. Original Experiments

The research started with the collection of rubble samples to be used for the experiments. After they had been collected, they were put in a copper tube and then placed in a high-temperature pressure vessel that had specifically been built to perform the experiments. A schematic of this vessel is presented in Figure 1.1. It consists of an outer and inner tube into which the copper tube which holds the samples can be put. On both sides of the samples, the tube is filled with ceramic grains with a size of 2 mm, which ensures the free gas flow and prevents the buckling of the copper at the transition between the hot and cooler sections of the oven (Wolf, 2006). This copper tube is then connected to a gas inlet and outlet, which is in turn connected to several measurement devices like flow meters, thermocouples and pressure/displacement transducers (Wolf, 2006). These allow for precise pressure and temperature monitoring and adjustment of the furnace intensity or gas pressure if needed. The gas used to create the annular pressure for the compaction is nitrogen, though other gases could also be used.

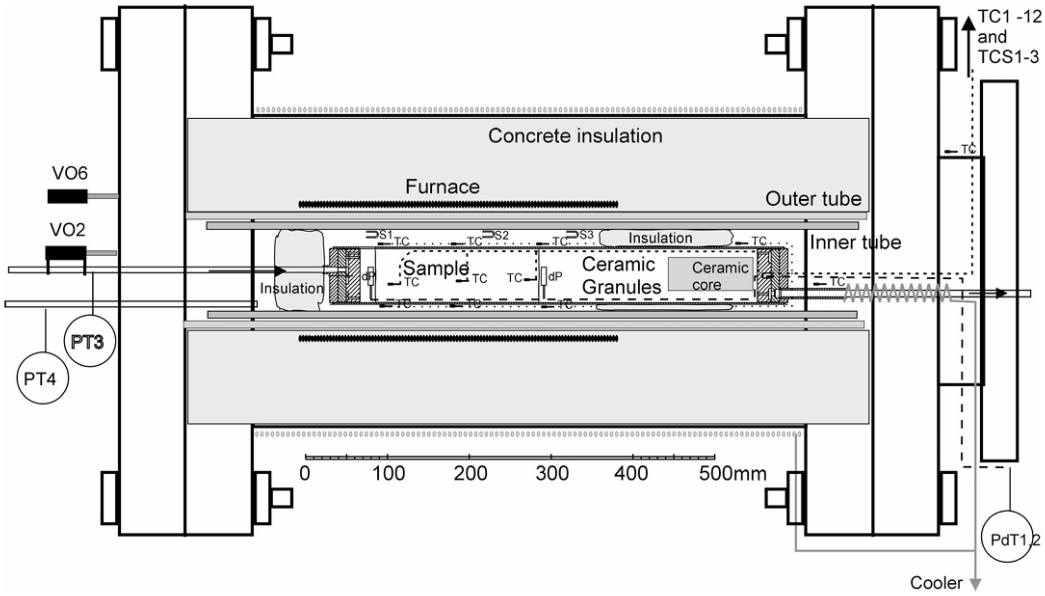


***Figure 1.1:*** *Cross-section of the vessel for the thermal treatment at high pressures of the rock samples used during the original experiments by K.H.A.A. Wolf. Adapted from Wolf (2006).*

The experiments usually lasted about 2 days (as long as there were no leakages or other safety hazards), during which the temperature, pressure and expansion were continuously recorded in graphs. All these data are still available. After the oven is switched off and the copper tube cools down, it is taken out. Figure 1.2 shows how different temperatures and pressures affect the tube and specifically the section that contains the sample. The tubes were then prepared for image analysis. This was done by first impregnating the tube with an epoxy, to prevent the rubble matrix from falling apart (Wolf, 2006). A fluorescent dye or colouring was mixed in with the epoxy to later aid in the discrimination between grains and pores.

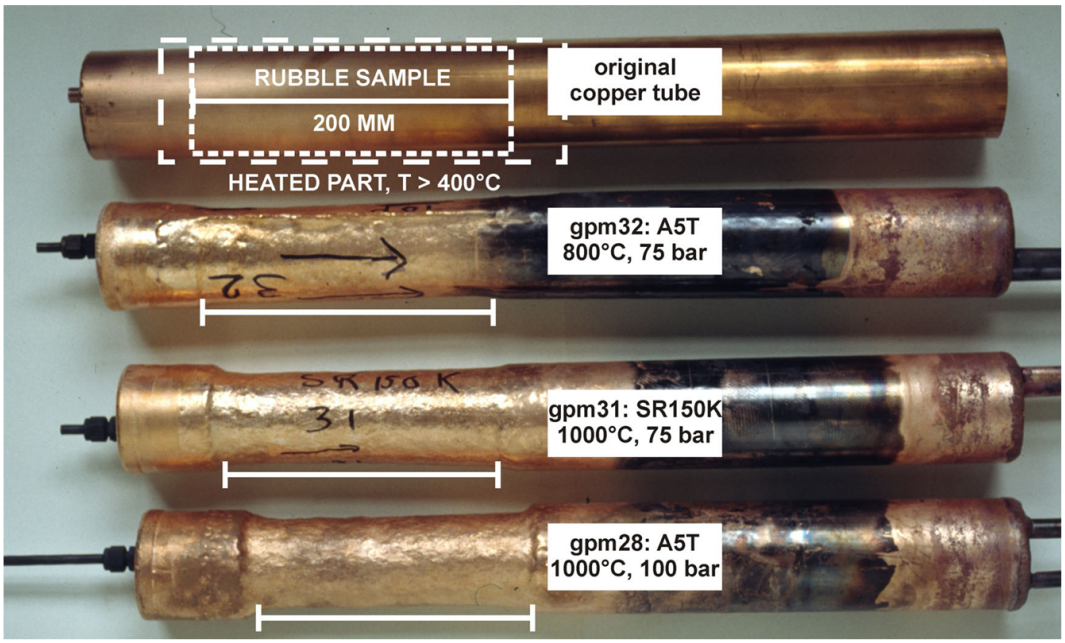


***Figure 1.2:*** *The original copper tube along with three tubes that underwent a treatment in the high-temperature pressure vessel. Adapted from Wolf (2006).*

A coating was added to the slabs after they were polished. The goal of this was to counteract the "Holmes effect". This is when the image of a component appears to occupy a larger area of the surface than it actually does, because the observer is able to see part of the 3D structure (Mandarim-de-Lacerda, Fernandes-Santos, and Aguila, 2010). A cross-section of a sample with and without a coating can be seen in Figure 1.3. By adding the coating, there is no need to apply a mathematical correction for the Holmes effect, thus increasing the accuracy of the results.

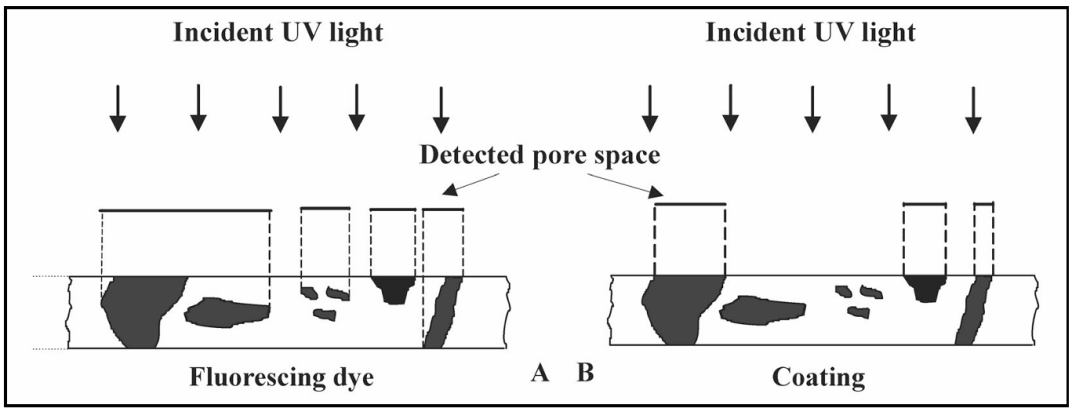


***Figure 1.3:*** *A: A section through an uncoated surface exhibiting the Holmes effect. B: A section through a coated surface showing the true 2D area size. Adapted from Wolf (2006).*

# 2 Methodology

The following chapter describes the methodology which was followed to quantify the porosity and permeability. Section 2.1 describes where the rubble samples were taken from and how they were classified into series. This is followed by an explanation of the equations used for the porosity and permeability calculations. The sections after this delve into the sample preparation and the experimental setups. The final sections of this chapter look into the methodology of image processing, both for digital photographs and $\mu$CT data. It describes which steps are taken to get an image that is as accurate as possible and the challenges related to each of these steps.

## 2.1. Sample Origins

The work by Wolf (2006) aims to understand the interaction between underground coal fires and their roof rocks. These events happen all over the world and lead to the emission of pollutant gases as well as danger to humans (J. J. Wu and Liu, 2011). Recent studies are still looking into methods of detecting and modelling such fires (Wang et al., 2023), as they have still not been fully understood. Wolf's study focuses on coal fires that combust spontaneously under natural conditions and include seams, floor rock, and overburdens (so-called natural coal fires). Throughout the research, many sites were visited, including China, Indonesia and Australia. For the laboratory experiments, two types of coal-related roof rock sediments were sampled: Westphalian coal and coal-related sediments from Northern Belgium and The Netherlands and Albian-age coal-related roof rock sediments from the Teruel Province in Spain. Some of them were only used for visualisation and mineralogical analysis, however, what is of interest to this study are the grain aggregates that were put into cylindrical tubes and later used in the experiments described in section 1.2. The samples were sorted into series based on their origin and composition as seen in Table 2.1.

***Table 2.1:*** *Sample series created for the original image analysis experiments.*

| Series | Age | Sediment Type | Origin |
|---|---|---|---|
| SR-150i-series[1] | Carboniferous | Laminated Siltstone | Beringen and Zolder (Belgium) |
| SR-150K-series | Carboniferous | Shaly Siltstone | Beringen and Zolder (Belgium) |
| 8670-series | Carboniferous | Silt Laminated Shale | Beringen and Zolder (Belgium) |
| A-series | Cretaceous | Silty Claystone | Open Pit Mines (Spain) |
| Pit-series | Cretaceous | Carbonaceous Silty Clay Shale | La Pitara Outcrop (Spain) |

Though the SR-150- and 8670-series are both Albian sediments from the same location, the difference is that the SR-150-series originates from a depth of 738 m and is from the Middle Westphalian, while the 8760-series is from a depth of 745 m from the Lower Westphalian (Wolf, 2006). The difference between the A- and Pit-Series is in the sampling location. Wolf (2006) describes the geological origin, petrography and geochemistry of these samples in more detail

[1]The SR-150i-series was not used for image analysis due to the poor quality of the preparations.

in Chapter 4. For this thesis, no new samples were used, rather the samples from Table 2.1 were revisited as they have been preserved.

## 2.2. Governing Equations

The porosity and permeability of a rock are two very important properties which have implications on the amount of fluid that can be trapped in a rock and the flow through it. Porosity is a very simple concept: it describes the percentage of rock volume that consists of pore spaces. In this thesis it is not volumes that are dealt with, but areas. Underwood (1970) suggests that the image porosity can be simply described as the pore area over the total area:

$$\phi_{IM} = \frac{V_p}{V_b} = \frac{A_p}{A_t} \tag{2.1}$$

To find it from a 2D section, a method has to be developed to discriminate between the pore and the grain area. The methodology behind this will be explained in section 2.5. The permeability is more difficult to determine. It is described as the ability, or measurement of a rock's ability, to transmit fluids (SLB, 2025). Since flow happens in 3D and there is no way to quantify permeability in 2D exactly, a formula has to be used to estimate the permeability of a rock from an image. The formula that will be used in this paper (Equation 2.4) is a modified version of the Kozeny-Carman relationship for permeability:

$$k_{KC} = \frac{\phi^3}{5(1-\phi)^2 S_0^2} \tag{2.2}$$

Where for the shape factor ($S_0$) the following relation is used:

$$S_0 = \frac{4}{\pi}\frac{P_p}{A_p} \tag{2.3}$$

This is a general shape factor used for the translation from 2D to 3D taken from Underwood (1970). It would not make sense to use a more complicated shape factor, due to the randomness of the grains and the very nature of morphology in which the geometrical structure, or texture, is not purely objective (Serra, 1982). The equation then becomes:

$$k_{KC} = \frac{\phi^3}{5(1-\phi)^2 \left(\frac{4}{\pi}\frac{P_p}{A_p}\right)^2} \tag{2.4}$$

Although the Kozeny-Carman relation is widely used and accepted to calculate the permeability of porous materials (Yin et al., 2022), it has one serious drawback: it does not take the pore size distribution into account, instead using only the average pore perimeter and area. When using it with porous materials that contain a wide range of pore sizes, the results can deviate from reality (Marshall, 1957). Therefore, the right averaging method needs to be used for the shape factor calculation.

## 2.3. Sample Selection and Cleaning

Before the samples can be analysed, they need to be sorted and cleaned. They are sorted first based on their series (Table 2.1) and then on the maximum temperature reached during the experiment in an ascending order. The sample names all start with GPM, which stands for *Gruis Permeabel Materiaal* (Dutch for *Grit Permeable Material*). The numbering refers to which experiments were performed first, which is irrelevant for this research.

***Table 2.2:*** *Samples analysed, sorted by series and maximum experimental temperature (low to high).*

| 8670-series | SR-150K-series | A-series | Pit-series |
|---|---|---|---|
| GPM61 | GPM34 | GPM35 | GPM60 |
| GPM54 | GPM12 | GPM36 | GPM59 |
| GPM63 | GPM37 | GPM39 | GPM58 |
| GPM53 | GPM19 | GPM33 | GPM57 |
| GPM52 | GPM40 | | GPM56 |
| GPM62 | GPM30 | | GPM55 |
| GPM51 | GPM17 | | GPM49 |
| | GPM31 | | GPM44 |
| | | | GPM45 |
| | | | GPM42 |
| | | | GPM46 |
| | | | GPM50 |
| | | | GPM48 |
| | | | GPM47 |

Since the samples had not been used in decades, they had collected some dust. The plan was to clean this off with a water and ethanol mixture. However, when cleaning a small part of the sample, it was noticed that part of the fluorescent coating came off. It was therefore decided to use a dry, microfibre cloth instead, as it got rid of the dust without potentially damaging the coating. The samples were then placed in the lab in the order described in Table 2.2, so they could be easily accessed for photography.

## 2.4. Experimental Setup

Two types of data were used for this thesis: photographs and CT scans. Two different setups had to therefore be built and used; they are described in the following subsections. The photography setup was used for all samples in Table 2.2, CT-scanning was only applied to selected samples.

### 2.4.1. Photography

A setup was built in the lab to take pictures of the rock samples. A schematic drawing of this setup can be seen in Figure 2.1. It consists of a table with a black cloth that limits reflection onto which the samples can be placed. On both sides of this table raised sections are built in between which a UV light source can be placed. Behind the table, a gallows pole with a height-adjustable camera mount is placed and a DSLR camera is mounted to this.

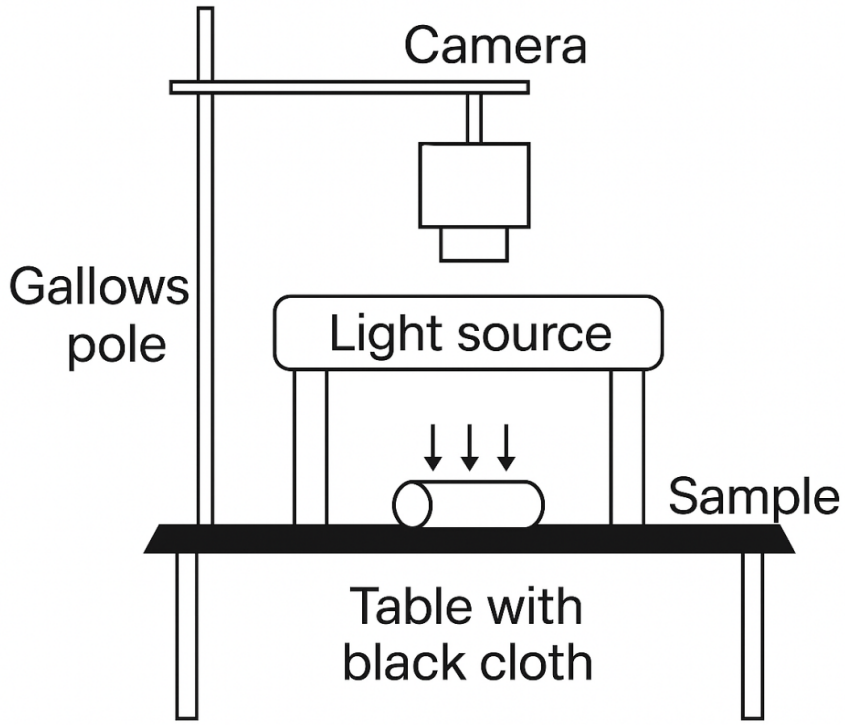


***Figure 2.1:*** *A schematic drawing of the setup used to photograph the samples.*

The camera used was the Canon EOS 600D combined with a lens with a focal length of 55 mm. An ISO value of 1600 and an aperture of f/6.3 were used. The camera was lowered as much as possible on the gallows pole to get a close zoom of the samples while maintaining sharp images. Small adjustments to the sharpness were made by manually adjusting the focusing ring on the lens and the exposure times were varied depending on the type of lighting used and the response of the uv dye. This was done with a trial-and-error technique. The samples fit once within the image frame widthwise and 3 times lengthwise, with some overlap. The pictures were then labelled with the sample number (e.g. GPM12) appended by L, M or R for Left, Middle or Right accordingly. As could be seen in Figure 1.2, the higher the temperature and pressure the samples were subjected to, the more the copper tubes were compressed. This resulted in different diameters for the samples and thus different thicknesses after they were cut in half. Therefore, for every sample one extra picture was taken with a scale bar, which would later be used to set the scale in the image processing software, ultimately resulting in 4 photos for every sample.

Figure 2.2 shows the setup for the UV light and the white spotlight. Due to the setup of the UV light there is a gradient from the top to the bottom, where the top of the sample is brighter. This is unavoidable when using just one UV light, but it is not problematic for the samples with a strong uv dye response, because the contrast between the grains and pore space is very significant. For the pictures taken with white light, a spotlight with more diffused light coming from 2 bulbs was used. The exact model of the spotlights used is the Leica CLS 150, with the light set to the maximum brightness and the colour set to imitate daylight. The use of the spotlights eliminates the gradient on the samples, thus making the image processing significantly easier and more accurate.

***Figure 2.2:*** *The setup with the UV light (left) and with the spotlight (right).*

### 2.4.2. CT Scanning

Computed tomography scanning is a technique which uses X-rays to visualise an object in 3D by scanning it slice by slice (Ache, 2022). Micro CT scanning is similar to medical CT scanning, with the difference that it can only be applied on a small scale. The benefit is that the resolution is much higher, which allows for the internal distribution of pores and grains to be visualised (Al Marzouqi, 2018).

The scanner consists of 3 parts, as shown schematically in Figure 2.3. The sample sits on a platform which can be moved from side to side, up and down and rotated. An X-ray source generates radiation, which passes through the sample and is recorded by a detector. The sample is then rotated and another image is taken- this is repeated many times until the entire sample is imaged (Ache, 2022).

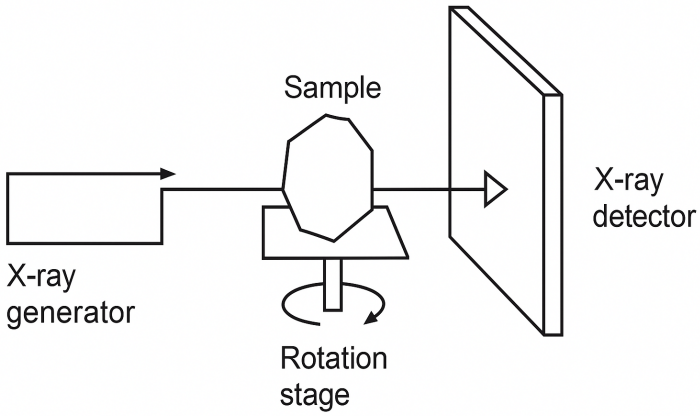


***Figure 2.3:*** *A schematic drawing of the $\mu CT$ scanner.*

The $\mu CT$ scanner used here is the Tescan CoreTOM. Figure 2.4 shows what the scanner looks like from the outside and the inside, with the three main components: the x-ray generator, detector and rotation stage containing the sample.

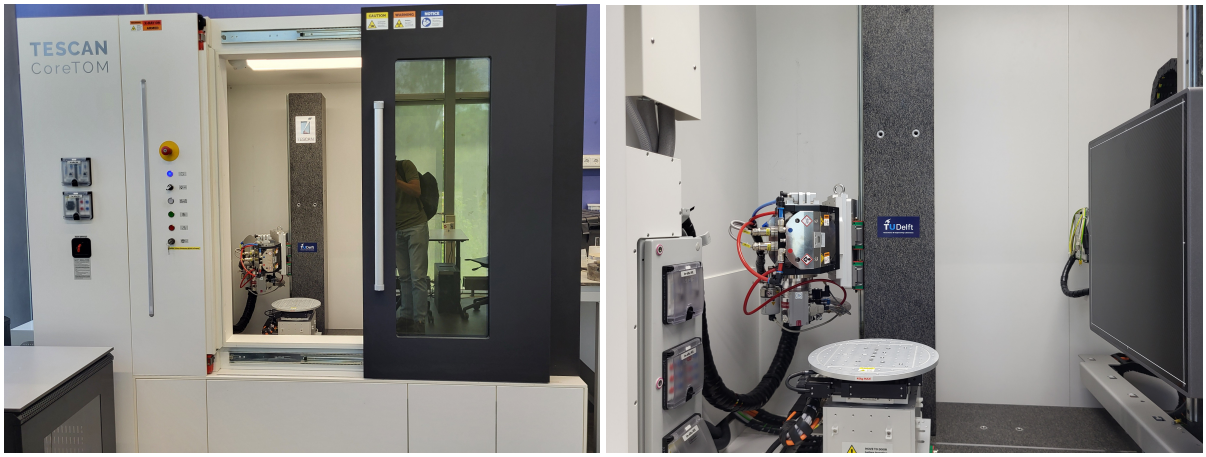


***Figure 2.4:*** *The μCT scanner used to scan the samples.*

## 2.5. Image Analysis Process

Porosity and permeability are 3D rock properties, while the examined slices are 2D. The field of study that deals with revealing the three-dimensional structure based on two-dimensional images is called stereology (Russ, 1986). It comprises many different steps, explained in the following subsections, ultimately aiming to differentiate between different objects- in this case, the grains and pore space. For this project, the image processing is done using Adobe Photoshop CS6 and FIJI (ImageJ).

### 2.5.1. Scale Setting

Knowing the scale of an image is crucial not only to apply the porosity/permeability formulas, but also to convey to others what the order of magnitude of the samples is. To achieve this, a ruler is put on each of the samples that can later be tracked in ImageJ using the *Line Segment* tool. Then, using the option *Set Scale* under the *Analyze* menu, the scale can be set (Figure 2.5). It is crucial to reset the scale for every sample, as differences in the sample thickness lead to them being at different distances from the lens, thus the magnifications being different.

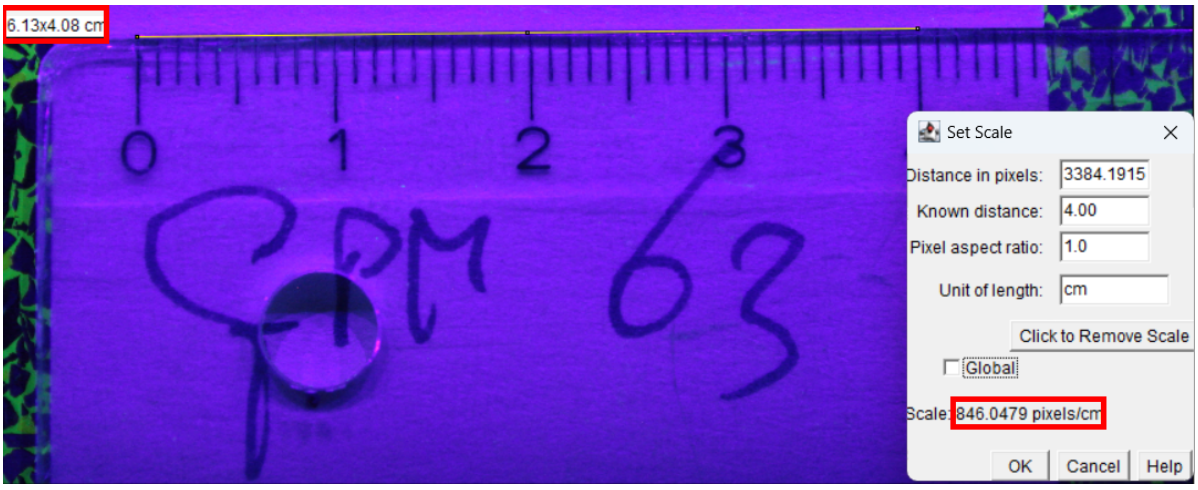


***Figure 2.5:*** *Setting the scale for the GPM63 samples in ImageJ. The ruler is tracked and this distance is then converted into pixels per centimetre.*

The RAW images without the scale bar are then opened in Photoshop and the image size is set under *Image* ⇒ *Image Size...* ⇒ *Document Size* as seen in Figure 2.6.

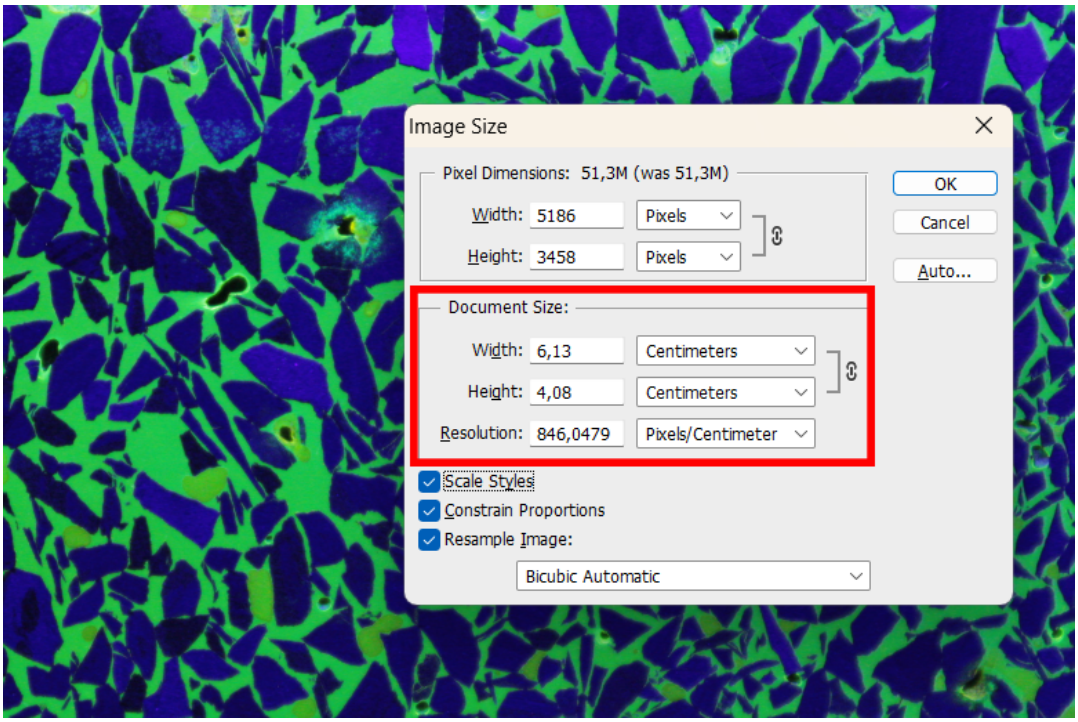


***Figure 2.6:*** *Setting the scale for GPM63L (UV) in Adobe Photoshop. The values in the red frame need to be filled in manually.*

### 2.5.2. Contrast

The goal of image processing is to achieve as large of a contrast as possible between the grains and the pore space. This can be done by using different light sources/camera settings (hardware) or with the use of software. Figure 2.7 shows the effect that a light source can have on the image quality. The image shot with just daylight and ceiling light has a gradient throughout the image which makes thresholding very difficult. The contrast between grains and pore space is also less pronounced, because the light is not uniform.

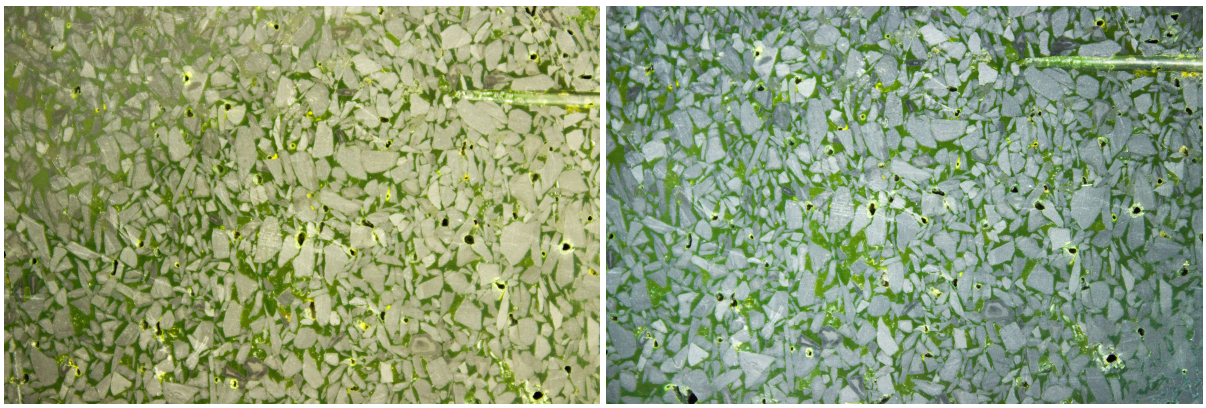

***Figure 2.7:*** *A photograph of GPM61M with only daylight and ceiling lights (left) and with the spotlights (right).*

Regarding the software, the contrast must be enhanced as much as possible, while keeping the amount of human interventions to a minimum and making sure it is repeatable. This automatically disqualifies all changes that require a human to judge what "looks better". The methodology that was ultimately chosen consists of two steps. Firstly, the RAW image is imported into Adobe Photoshop and *auto* is chosen in the menu that pops up. The software automatically adjusts the exposure, contrast, whites and blacks. Secondly, in the menu on the right, the *Black & White* adjustment is selected, which changes the image to greyscale.

These operations make the grains more distinguishable from the pore space, thereby increasing the accuracy of the area and perimeter measurements later on. The greyscale filter helps eliminate unwanted details, like colours of minerals or paint marks and prepares the image for thresholding, which does not use colours. The effects of this can be seen in Figure 2.8.

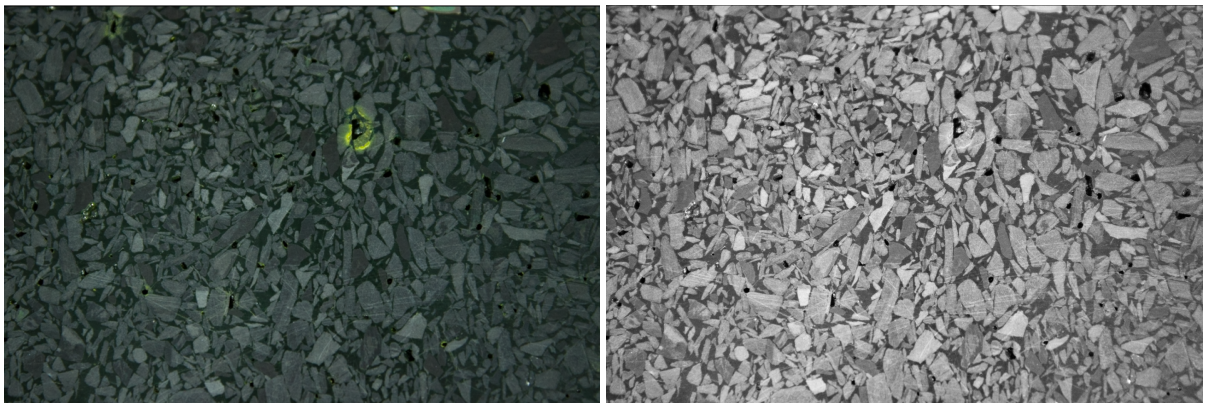

***Figure 2.8:*** *The original photograph of GPM54M (left) and the same picture after applying automatic brightness/contrast changes and making it greyscale in Adobe Photoshop (right).*

### 2.5.3. Image Size and Averaging Techniques

The spotlight works well in preventing a top-to-bottom gradient in the photographs, but a vignetting effect is still present and can be seen slightly in Figure 2.8. Vignetting in photography refers to the loss of light in parts of the image due to the blocking of a part of the incident rays (Yu, 2004). It appears as a gradual fading at the edges of an image, most pronounced at the corners. It causes problems in the discrimination between grains and pores, since the threshold needs to be set at a specific brightness level. Brightness differences mean that grains near the edge might have the same brightness as pores in the middle of the image.

It is possible to apply some manual corrections to remove the vignetting effect, but this goes against the principle of keeping the whole process as simple and repeatable as possible. Instead, the possibility of picking a Representative Elementary Volume (REV) was explored. By taking just a part of the image, the areas affected by vignetting can be avoided, and as long as the area is big enough and representative of the whole sample, the measurements should be valid. To test if zooming in to get a smaller REV would indeed work, the porosity and permeability were measured with a full-size image and with fractions of this image. To exclude human biases, this was done by taking half of the image every time (going into the top left corner). The results of this procedure on the porosity are presented in Figure 2.9.

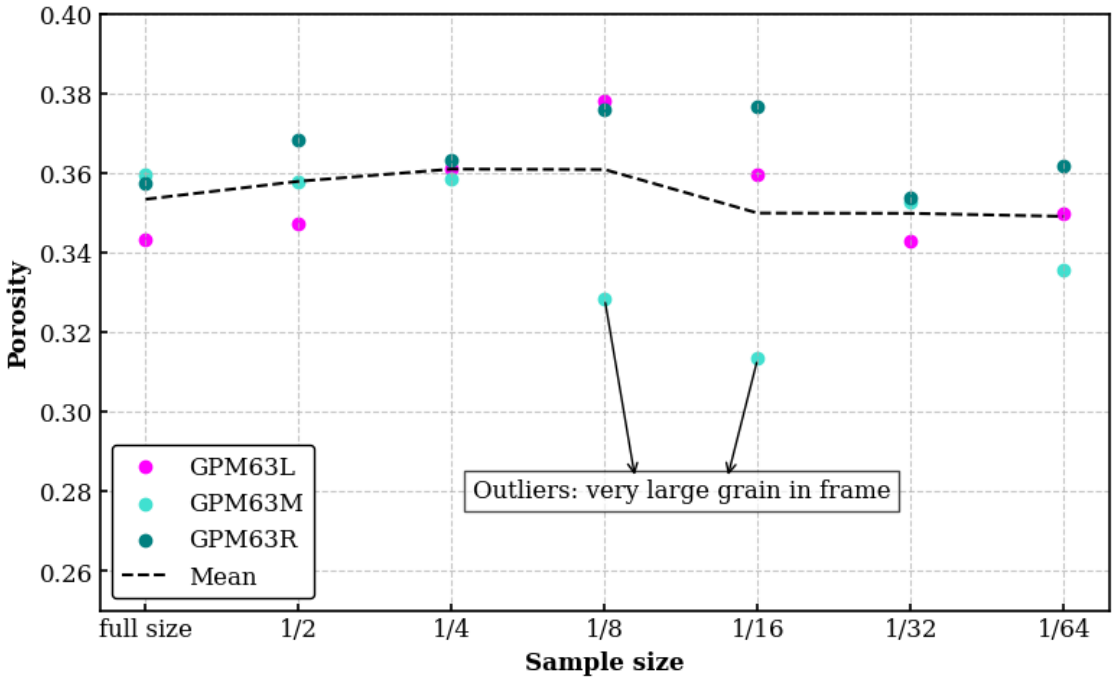


***Figure 2.9:*** *The calculated porosity for increasingly smaller parts of photographs of the GPM63 sample taken with UV lighting.*

As can be seen, the porosity remains rather constant throughout. The only two outliers for $1/8$ and $1/16$ of the total size of GPM63M are caused by an unusually large grain being present in that part of the image. When looking at just the porosity, the conclusion would be that the REV is equal to or smaller than $1/64$ of the image size. This is due to the porosity calculation depending on only the ratio between grains and pores (black and white in a binary image) and the grains being distributed homogeneously.

The permeability calculation depends on two more variables: the pore area ($A_p$) and pore perimeter ($P_p$). The ratio between these forms the basis of the shape factor (Equation 2.3). Two different averaging techniques can be used to calculate this ratio, leading to vastly different results. The first method sums all the pore perimeters and then divides by the sum of all pore areas. This is the same as taking the arithmetic mean of all pore perimeters over the arithmetic mean of all pore areas, as the averaging calculation (dividing by $N$) cancels out by being in both the numerator and the denominator of the main fraction (as seen in Equation 2.5).

$$S_0 = \frac{4}{\pi} \frac{\sum_{i=1}^{N} \frac{P_{p,i}}{N}}{\sum_{i=1}^{N} \frac{A_{p,i}}{N}} = \frac{4}{\pi} \frac{\sum_{i=1}^{N} P_{p,i}}{\sum_{i=1}^{N} A_{p,i}} \tag{2.5}$$

The second method takes the mean of the **individual** ratios, meaning that the $P_p/A_p$ ratio of each pore contributes equally to the final outcome. This results in Equation 2.6.

$$S_0 = \frac{4}{\pi} \frac{1}{N} \sum_{i=1}^{N} \frac{P_{p,i}}{A_{p,i}} \tag{2.6}$$

To see which averaging technique is more suitable for the permeability calculation, both were implemented for the 3 pictures (L, M & R) of GPM63 UV. The results are visible in Figure 2.10.

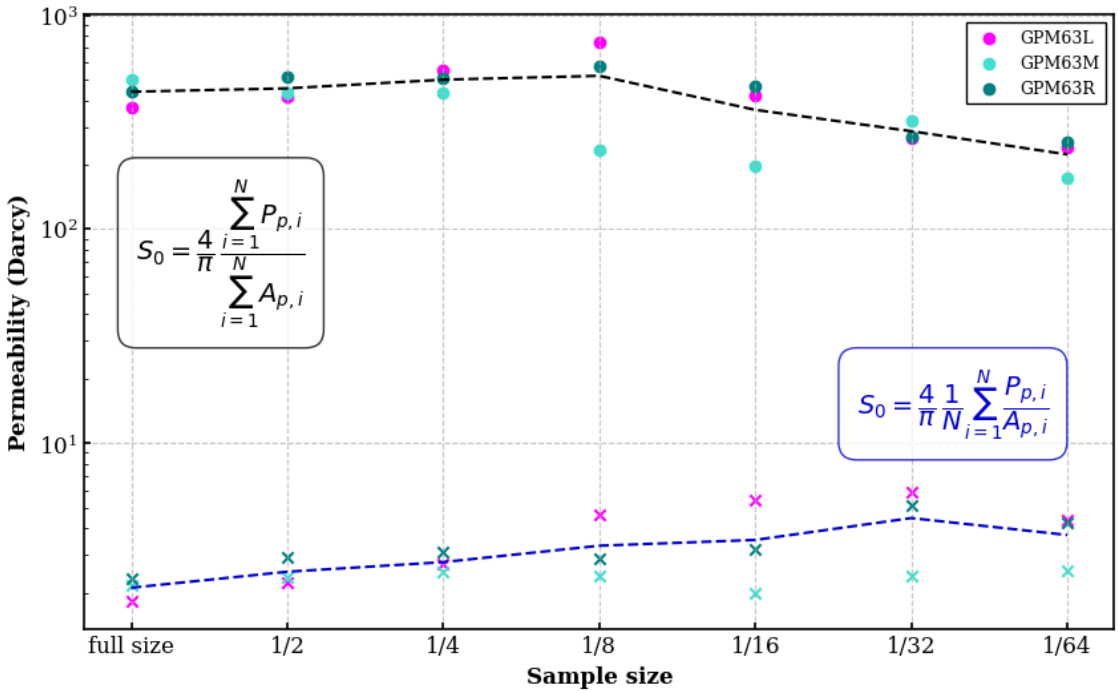


***Figure 2.10:*** *Two averaging techniques applied to calculate the permeability for increasingly smaller parts of photographs of the GPM63 sample taken with UV lighting.*

The first method corresponds well to the permeability values found by Wolf (2006), who noted an experimental permeability of 255 Darcy and Image Analysis permeabilities ranging from 608 to 831 Darcy. The discrepancy with the second method is two orders of magnitude. Mathematically, this can be explained by the fact that each pore contributes equally to the ratio in the second method, regardless of its size. This leads to an over-representation of the small pores, which do not affect the permeability as much, according to Luo et al. (2024). They found that middle-sized pores have the largest effect on permeability, with very small and very large pores being less important. Moreover, small inaccuracies in the image processing lead to many tiny spots being classified as pores, while they are parts of a grain. Thus, the first method, delivering a weighted result and emphasising the importance of middle-sized and larger pores, is preferred.

So, the first conclusion from Figure 2.10 is that averaging method 1 (Equation 2.5) should be used in the Kozeny-Carman permeability calculation. The second conclusion is that the REV is 1/8 of the image size, as the permeability is relatively constant until this point and follows a downward trend after it. Having determined this, the image size can now be reduced to combat the vignetting effect in the white light images and the top-to-bottom gradient in the photographs taken with UV light.

The size of the original pictures is around 6 $cm$ in width and 4 $cm$ in height, resulting in an area of roughly 24 $cm^2$ being covered. With the REV being 1/8 of the image size, it would be possible to reduce the image to just 3 $cm^2$. However, the more the image size is reduced, the more the images are affected by heterogeneities; Figure 2.9 shows the danger of outliers being more pronounced in smaller fractions of the image. Moreover, reducing the image size

to 1/4 of the original would already suffice for removing the vignetting effect (as long as the image size reduction was done by *zooming* into the centre of the photograph). Hence, it was decided to reduce all images, regardless of their exact initial dimensions (W: 5.90-6.33 $cm$ / H: 3.93-4.22 $cm$), to a width of 3 $cm$ and a height of 2 $cm$. Keeping the dimensions constant has an advantage at a later stage as well, as it means that the image dimensions then do not need to be changed for every image in the code (Appendix A).

Reducing the image size is done in Adobe Photoshop. After the scale is set, the canvas size option has to be selected under *Image* ⇒ *Canvas Size...*. All that has to be done is to fill in the desired size and the programme will zoom exactly into the middle of the image.

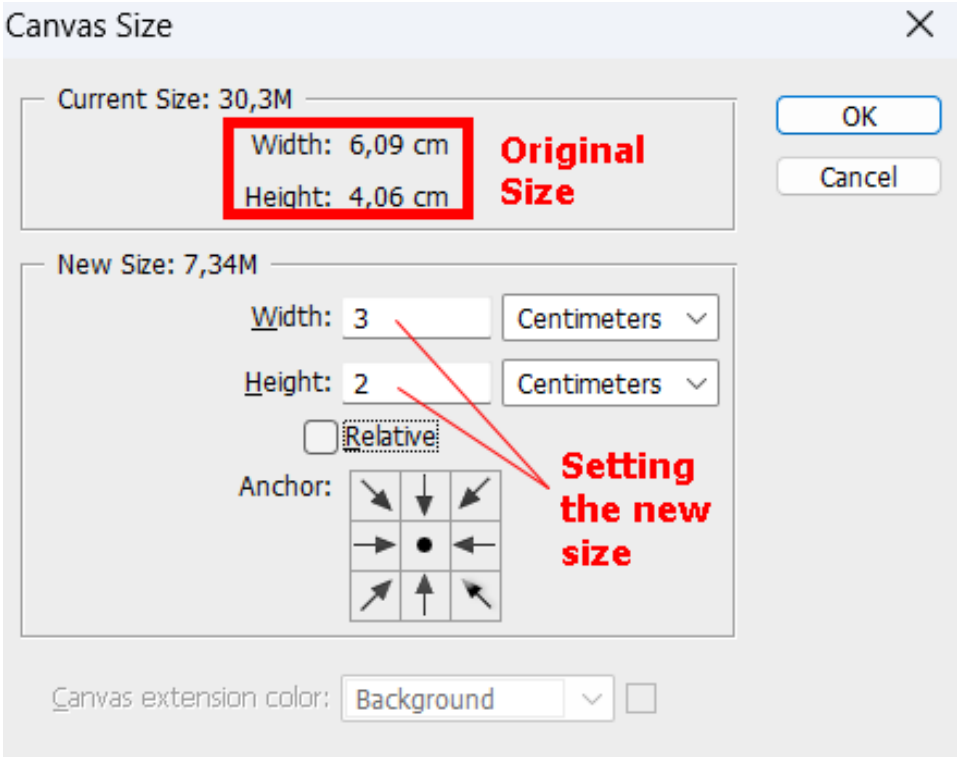


***Figure 2.11:*** *Reducing the image size in Photoshop.*

### 2.5.4. Segmentation

Segmentation in image processing refers to the partitioning of pixels into separate groups, in this case, grains and pores. Since the segmentation is done into just these two groups, the output is a binary image with only black and white pixels. Both the process of converting to a binary image and the processing of this image to get the grain and pore properties is easily done in ImageJ. It is crucial to do the preprocessing steps in Photoshop though, because the algorithm used to make the images binary can otherwise misidentify many of the grains as pores and vice versa.

The preprocessed, grayscale image is loaded into ImageJ and then the image type is set to 8bit under *Image* ⇒ *Type* ⇒ *8bit*, since there is no use in it being read as a colour image if it is made binary anyway. Under *Process* ⇒ *Binary* ⇒ *Make Binary* the image is then segmented. Here, it is important to keep into account that the grains should become black and the pores white, as it is the pore area and perimeter which are needed for the KC-permeability calculations.

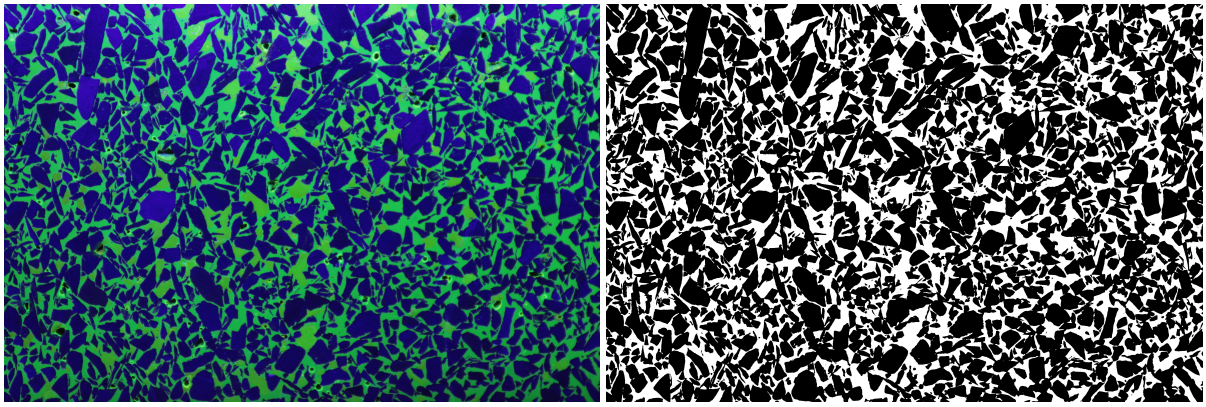

***Figure 2.12:*** *The original photograph of GPM63M and the same picture in binary form. The grains are made to be black and the pores white.*

The quality of the binarisation depends on three factors:

1. The quality of the sample and the dye impregnation
2. The lighting and camera settings
3. The post-processing of the images

The first one cannot be influenced, since the samples were already prepared before the start of this research. The lighting and camera settings should be set to maximise contrast as described in subsection 2.5.2. Post-processing is the last step, but it does not stop after the image has been binarised, as will be described in the next subsection.

### 2.5.5. Binary Image Editing and Modification

The binary images obtained after segmentation often contain defects and errors caused by the illumination, sample imperfections or noise. There are ways of letting a computer improve these via automatic routines. Two of the most common operations are erosion and dilation. These two operations aim to reduce the irregularities of the feature outlines, thereby reducing the perimeter. If this is not done, the area will turn out to be more or less correct, but the perimeter will be much too large (Russ, 1986). An erosion operation goes around a feature and removes every pixel that does not have the same value (colour) all around it. Dilation does the opposite; it turns an ”off” pixel ”on” if one of the pixels around it belongs to a feature.

Dilations and erosions significantly increase or decrease the area of a feature if used on their own. A sequential use of these operations, however, will leave the area unchanged on average, while smoothing and decreasing the perimeter (Russ, 1986). If an erosion is followed by a dilation, then it is called **opening** and if a dilation is followed by an erosion, then it is called **closing**. Figure 2.13 displays how a binary image is affected by these operations.

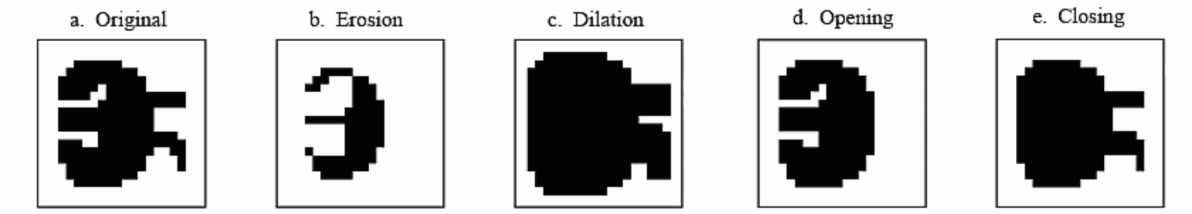


***Figure 2.13:*** *A binary image with four morphological operations. Adapted from Smith (1997).*

For the image analysis of grains, it is better to apply opening than closing. Firstly, because opening makes the border of a feature smoother, rather than extending features at the border like closing (Smith, 1997). Also, since grains do not typically have large holes or channels in them (like in Figure 2.13 (a)), even when accounting for noise, the result of an opening operation will yield smooth grains.

The question which then remains is how many ”open” cycles should be performed. When multiple cycles are done, a series of erosions is followed by the same number of dilations. If the binary image is unaltered, then the perimeter will be overestimated, which will lead to a higher shape factor and hence too low of a permeability. If too many cycles are applied, the grains will become almost square, reducing the perimeter to an unrealistically low value. Another problem with too many openings is that some small grains can get fully eroded away, therefore also affecting the area fraction and thus the porosity. The amount of ”open” cycles was experimented on with sample GPM61, as can be seen in Figure 2.14.

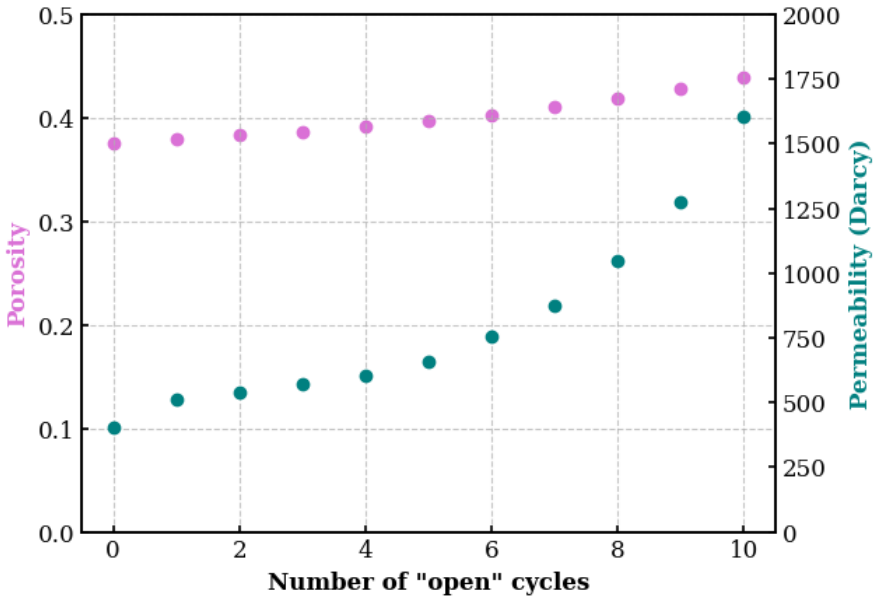


***Figure 2.14:*** *The effect of the amount of open cycles on the porosity and permeability of GPM61M.*

In the graph, there is a jump from none to one cycle, then the porosity and permeability remain relatively steady and start growing increasingly quickly after 4 cycles. From a look at this graph and at how the images turned out, it was decided to go for 2 ”open” cycles, as they would smooth the edges without altering the objects too much. This can be applied in ImageJ under *Process* ⇒ *Binary* ⇒ *Options...*, selecting 2 iterations, a count of 1 and option *Open*.

One last problem remains: many grains touch and are seen as one big grain rather than multiple smaller grains. The *watershed* option in ImageJ might seem like a solution: it draws lines between the grains (or between pore spaces, depending on the setting), dividing them into smaller parts. However, the algorithm behind this is not suitable for the purpose of discriminating grains or pore spaces from each other, as it draws too many lines. Figure 2.15 (right) shows why the watershed function **should not** be used. The middle image shows why 2 open cycles **should** be used, as they smooth the original binary image very well.

***Figure 2.15:*** *GPM63L binary (left), with 2 open cycles (middle) and watershed (right).*

So, the watershedding does not work and many grains are still connected and seen by the programme as one big grain. While this is not ideal, it is not a very big issue, because the perimeters and areas are still very close to what they should be and the averaging technique that is used (subsection 2.5.3) is not dependent on the amount of grains anyway.

### 2.5.6. Step-by-step Process

Taking into account all the processes described in the paragraphs above, the final image analysis methodology can be summarised in the following steps:

1. For the sample to be analysed, open the picture with the ruler in ImageJ, use the line tool to trace the ruler, select *Analyze ⇒ Set Scale...* and fill in the known distance (the distance traced by the line segment tool). The distance in pixels should be automatically filled in.
2. Open the left, middle and right pictures in Adobe Photoshop or a similar photo editing software. Since the pictures are in RAW format, the programme will suggest some editing settings. Choose the *Auto* setting to let it enhance the colour brightness and contrast automatically. If prompted, choose the *Don't color manage* option.
3. Select *Image ⇒ Image Size*. In here, make sure to set the resolution to *Pixels/Centimeter* and fill in the values from step 1 as shown in Figure 2.5 and Figure 2.6.
4. Under *Image ⇒ Canvas Size...* reduce the size of the image to a width of 3 cm and a height of 2 cm in order to counteract the vignetting effect/ colour gradient resulting from the light source positioning.
5. In the *Adjustments* menu select the *Black & White option*. This makes the image greyscale. Choose the *Auto* option to change the influence of different colours, this will increase the contrast. If it is the case that the contrast is still insufficient and it is a UV-photograph (which uses green dye and makes the grains look blue), reducing the slider of the "Blues" to the minimum value will help increase the contrast further.
6. Save the images as TIFF files, make sure to name them according to the naming convention (e.g. GPM63L, GPM63M, GPM63R) and when saving, choose to *Discard Layers*.
7. Open the images in ImageJ. Check if they are the right size (3 by 2 cm).
8. Choose *Process ⇒ Binary ⇒ Make Binary*, making sure that the grains are black and the pores white. This is because the pore areas and perimeters are of interest in the later calculations and should therefore be assigned the binary value of 1 (white).
9. Under *Process ⇒ Binary ⇒ Options...* select 2 iterations, a count of 1, mark the *Black background* checkbox and under *Do:* choose *Open*. This will perform 2 erosions followed by 2 dilatations.

10. In the *Analyze* menu, tick the boxes with *Area* and *Perimeter* under *Set measurements...*. Then, choose *Analyze* ⇒ *Analyze particles...* and save the results as a .csv file.
11. Open the .csv file in the python code from Appendix A, run it and the results will be saved in an excel file. This file can then be used to create plots.

## 2.6. CT Scanning Process

The micro-CT scanner outputs its data as a series of 2D slices, which can be stacked to create a 3D visualisation of the rock sample. Because the samples are half-cylinders and it is easier to analyse rectangular slices (and later compare them to the 2D image analysis results), they are first imported and cropped in Photoshop. The file size of a single slice is reduced from about 7 MB to 2 MB. The first of the 2D images is opened and under *Window* ⇒ *Actions*, a new action is created. The image is then cropped using the *Canvas size* option to a height of 3 and a width of 2 cm (it was determined in subsection 2.5.3 that this is bigger than the REV). Next, choosing *File* ⇒ *Automate* ⇒ *Batch...* allows the just saved action to be automatically applied to all image slices.

The image slices are then imported into the Dragonfly 3D software (specifically version 2024.1 Build 1627). Here, in the segment menu, a range is defined for the segmentation; all values below this range are defined as pore spaces (as these show up darker in the CT scans) and all values above are defined as grains. The thresholding range can be automatically set using the Otsu algorithm. This method works by iterating through a series of threshold levels and tracking the spread of pixels below and above it, then selecting the optimum where the weighted spreads are minimal (Bangare et al., 2015). As described by Bangare et al. (2015) though, the drawback of this method is that it only depends on the intensity of the pixels and no other relationships are taken into account. This results in the issue illustrated in Figure 2.16, where the Otsu method misclassifies slightly lighter pixels (belonging to the grains) as pores, thereby overestimating the porosity. The difference in porosity values between manual and Otsu thresholding for GPM63 and GPM19 is just between 0.01 and 0.03. For GPM33 it is exceeds 0.90, since that sample has a very low porosity and the Otsu method sets the threshold at the boundary between lighter and darker grains instead of between the grains and pores. It is for this reason that the thresholding was done manually.

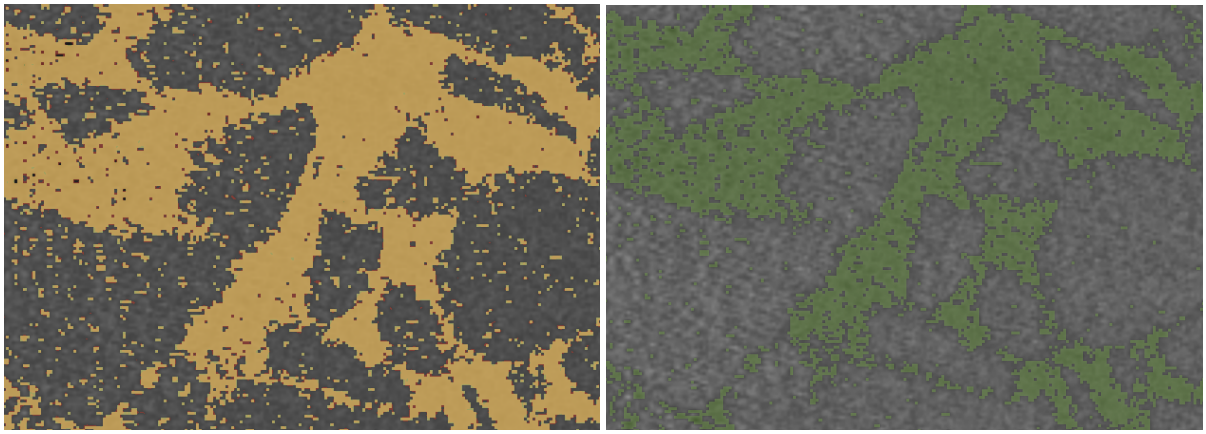

***Figure 2.16:*** *A comparison of the Otsu algorithm (pores are yellow) to manual threshold selection (pores are green) for a micro-CT scan of GPM19.*

The proper threshold value was selected as the point where the amount of grains classified as pores was (close to) equal to the amount of pores classified as grains. After choosing this value, the option *Add to New* creates the pore space as a new ROI (Region of Interest). Under the tab *Statistical properties*, the volume as a percentage of the total volume, which in this case is the porosity, can be found. This new ROI can also be visualised in 3D as shown in Figure 2.17.

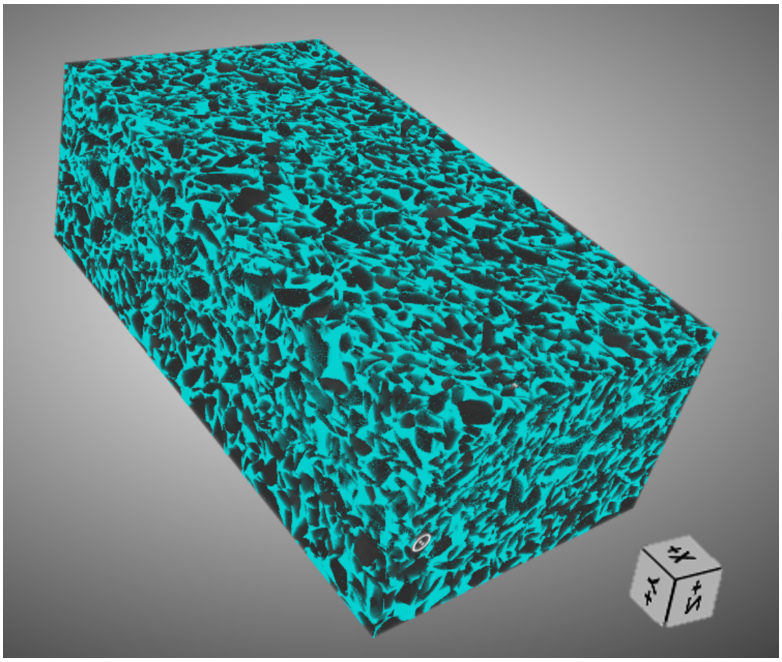

***Figure 2.17:*** *Part of GPM63 visualised in 3D using Dragonfly.*

Dragonfly 3D has the Porous Microstructure Analysis (PuMA) plugin (Comet Technologies Canada Inc., 2024), which can compute the permeability of a sample. However, due to the high resolution of the scans and hardware limitations, this could not be used. Instead, Equation 2.4 was transformed to a 3D counterpart, taking out the $\frac{4}{\pi}$ area correction and replacing the perimeter by the area and the area by the volume:

$$k_{KC}^{(3D)} = \frac{\phi^3}{c(1-\phi)^2 \left(\frac{S_p}{V_p}\right)^2} \tag{2.7}$$

The pore surface ($S_p$) and pore volume ($V_p$) were calculated in the statistical properties tab of the previously created pore ROI.

# 3 Results

This chapter presents the results of the image analysis and CT scanning. It starts with a section showing the effects of different light sources, answering the question of which one should be used. Afterwards, the image analysis results are discussed in terms of the effect of temperature on porosity and permeability. In the final section, the CT scanning results are discussed and a comparison of 2D and 3D is made.

## 3.1. Effect of Lighting

Before image analysis can start, the pictures need to be taken. Since the samples had been impregnated with a fluorescent dye, the first option explored was to photograph them with UV light. However, as seen in Figure 3.1, there were differences in what the samples looked like under a UV lamp.

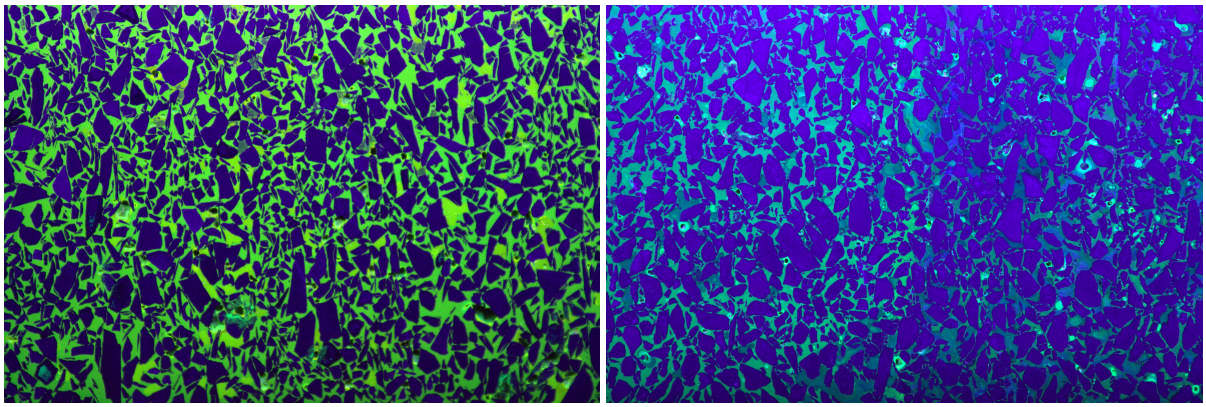

***Figure 3.1:*** *Samples GPM61L (left) and GPM34L (right) photographed with UV light.*

GPM61 was impregnated well, with the dye sitting in the pore spaces and contrasting with the grains. On the contrary, in GPM34, the contrast between the grains and pores is small, especially in terms of brightness. More important than the brightness difference is the variability in brightness, as the segmentation algorithm used in ImageJ chooses a threshold value on the greyscale version of the images, making all pixels lower or equal to the threshold value black and all above it white (Sparavigna, 2020). If the brightness differences between the grains and pores are **inconsistent**, i.e. sometimes the grains are brighter and sometimes darker than the pores, then difficulties in segmentation occur.

Figure 3.2 shows what samples GPM61 and GPM34 look like after applying the segmentation algorithm. Both sample pictures contain a gradient, in which the top is brighter than the bottom, resulting in grains being seen as pores in the top and vice versa in the bottom of the images. As discussed in subsection 2.5.3, this effect was eliminated by cropping the image. This, however, does not resolve the issues seen in the binarisation of sample GPM34, where the differences in brightness between the grains and pores are inconsistent.

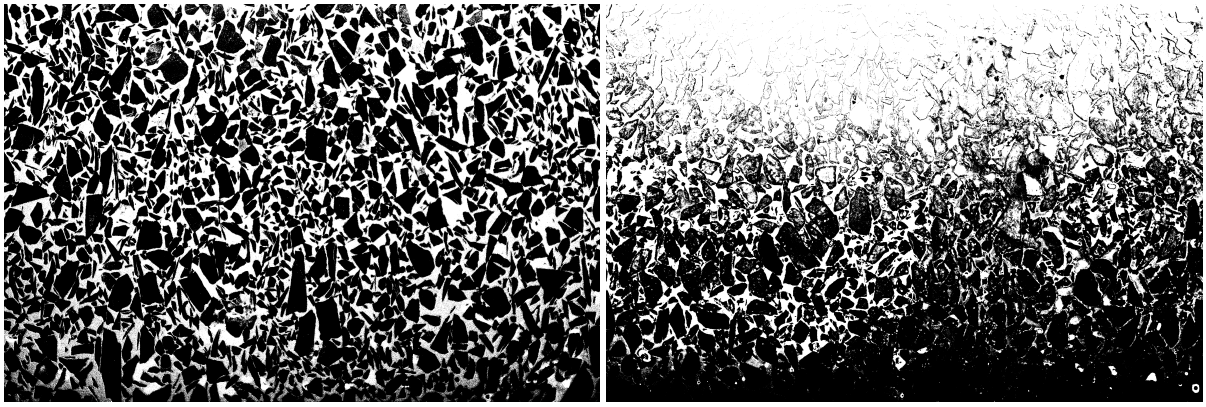

***Figure 3.2:*** *The samples from Figure 3.1 made binary without any preprocessing.*

There are two potential solutions: applying preprocessing to increase the contrast or taking pictures with normal light. The former is done according to the process described in the methodology. The most important step in this process is the conversion to greyscale- step 5 in subsection 2.5.6. The *Auto* option automatically sets different influence values to different colours, making the grains more distinguishable from the pores. For samples with very inconsistent brightnesses, like GPM34, a longer shutter time is required to allow more light into the sensor. Additionally, the slider for blue in the greyscaling option in Photoshop can be set to a minimum to increase the contrast between the green and blue parts of the image. As seen in Figure 3.3, this leads to a large enough contrast for the ImageJ thresholding to work well.

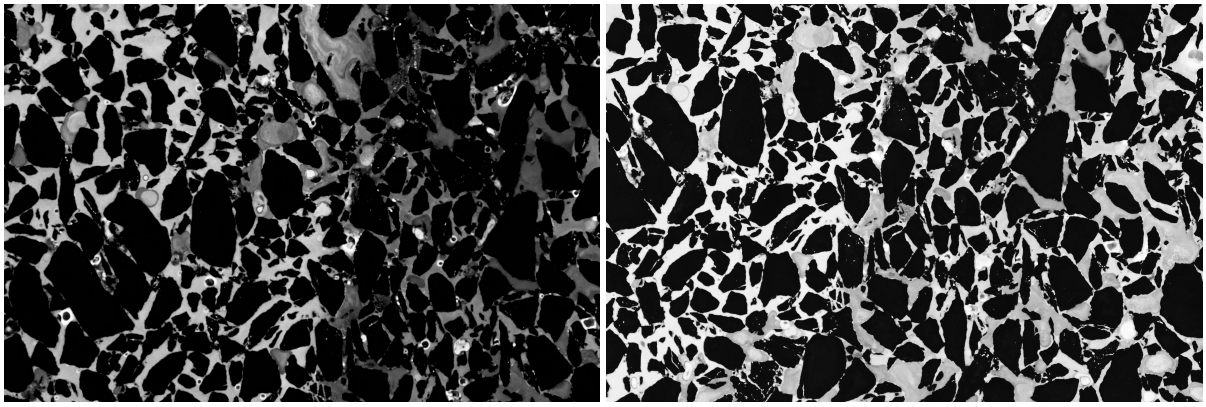

***Figure 3.3:*** *Sample GPM34L after preprocessing with the greyscale option (left) and after additional tweaking (right).*

The results of thresholding with the preprocessed sample images are shown in Figure 3.4. Compared to Figure 3.2, the grains are now clearly separated, making the images usable for image analysis.

So, for samples GPM34 and GPM61, the photographs taken with a UV light source turned out well, albeit after implementing some image processing techniques. The option of taking pictures with normal light still remains an alternative. If done, a bright and directional light source must be used to maximise the contrast, as mentioned in subsection 2.5.2. Another requirement is that there must be sufficient contrast between the grains and pore spaces, which varies significantly between the samples as seen in Figure 3.5.

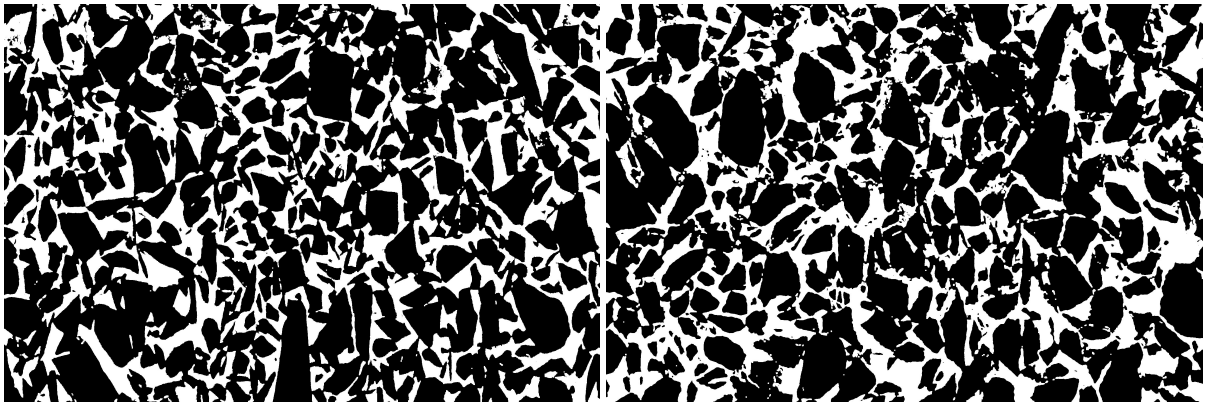

***Figure 3.4:*** *GPM61L (left) and GPM34L (right) shot with UV light after all processing steps.*

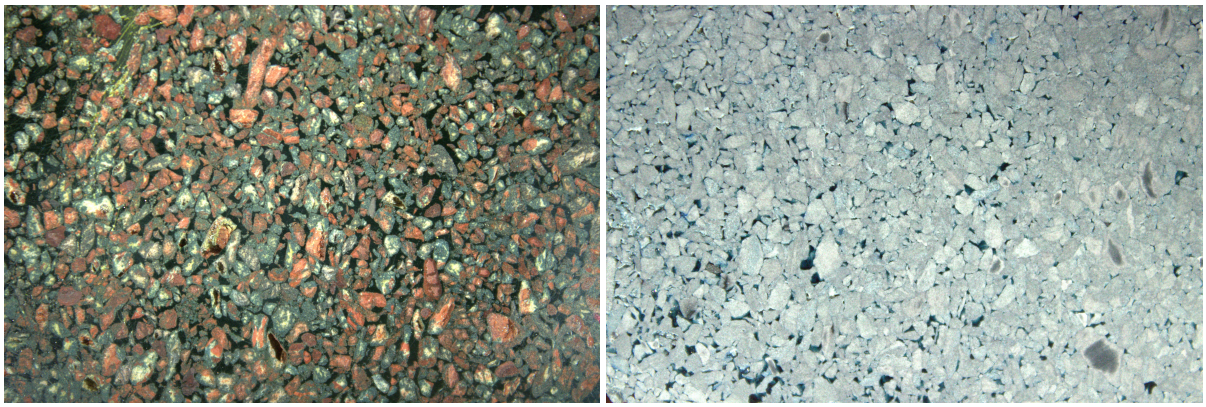

***Figure 3.5:*** *GPM60L (left, Pit-series) and GPM31L (right, SR150-series) shot with normal light.*

Both samples in Figure 3.5 were poorly impregnated with fluorescing dye, which limited the effectiveness of UV illumination. In GPM60, the pore space was distinguishable under normal lighting, but the many colours of the grains reduced the effectiveness of the greyscale filter for contrast enhancement. Despite the limited dye penetration, UV imaging yielded clearer results and was therefore used. For GPM31, however, imaging with normal light provided superior contrast and was used.

***Table 3.1:*** *Samples of which the photographs with normal light were used.*

| 8670-series | SR150-series | A-series | Pit-series |
|---|---|---|---|
| *None* | GPM19 | *None* | GPM48 |
| | GPM40 | | GPM47 |
| | GPM31 | | |

Of the 33 samples, only 5 had a higher contrast when photographed under normal light compared to UV light (Table 3.1). This was the case for poorly impregnated samples and samples for which the dye partly covered the grains. Regarding the coating, Wolf (2006) mentions that different components were tested over the years, finally choosing Caldofix$^{TM}$ with a bright yellow fluorescent dye. It is unclear if this was used for all 33 samples which were analysed

here, or if the differences in impregnation quality are a result of different coating compositions. What is obvious though, is that coating is an essential step and if done correctly with a fluorescing dye, pictures taken with a UV light source will always have an advantage over pictures taken with normal light.

## 3.2. Image Analysis Results

The main purpose of the image analysis is to determine the porosity and permeability of the samples. Figure 3.6 displays the porosity and permeability of all samples, with a separate graph for every sample series. The samples were sorted by temperature, where the sample on the left was subjected to the lowest maximum temperature. The exact temperatures can be found in Appendix B.

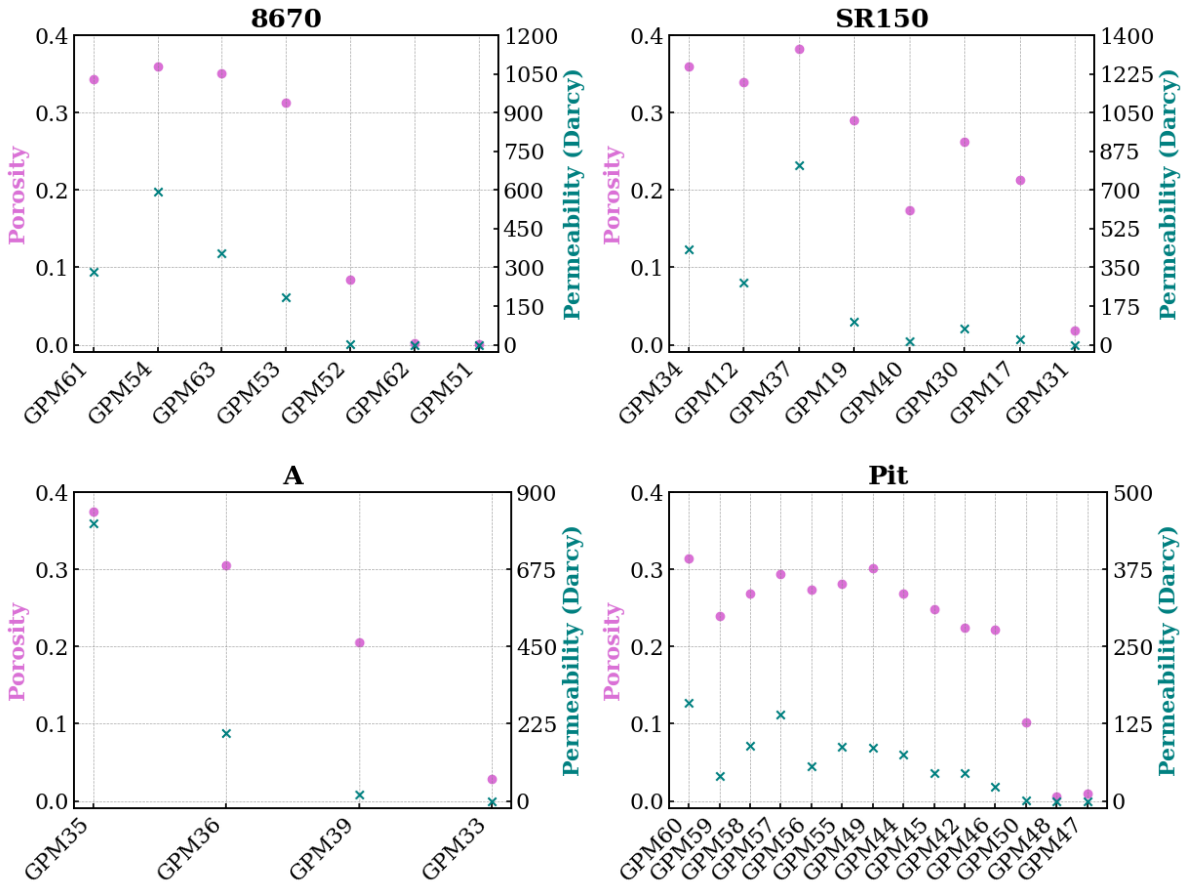


***Figure 3.6:*** *Porosity and permeability results for all samples, sorted by series.*

The graphs display a trend where the porosity and permeability decrease to the right side. This trend is best visible in the graph for the A-series, as it contains no inconsistencies. Some of the samples had issues which caused inconsistencies in the image analysis results, most notably GPM54, GPM37, GPM57 and GPM56. These samples were revisited to investigate why they do not follow the trend:

**GPM54** initially had a permeability of over 1000 Darcy, while the samples exposed to slightly higher and lower maximum temperatures had permeabilities of around 300 Darcy. This can

be partly explained by grains that have fallen out of the top layer of the sample after coating. Figure 3.7 shows the original part of GPM54R used for image analysis (with a missing grain) and the same picture, but cropped to a different part where no grain was missing. The average permeability of GPM54 when using the parts without missing grains is 492 Darcy, which is a more logical value considering the overall trend.

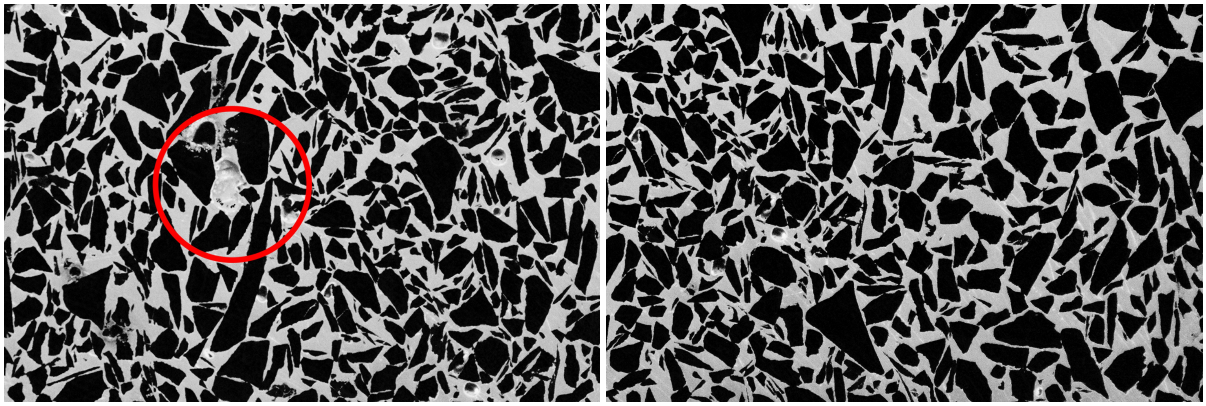

***Figure 3.7:*** *The originally used cropped picture of GPM54R with a grain missing and another part of the same picture without missing grains, which was then used.*

**GPM37** contains many irregularities. Although the UV dye shines through clearly, something happened during or after the impregnation process, resulting in a large number of holes and dark spots inside the epoxy. These could indicate grains that were partially covered by epoxy. The dark spots (top circle in Figure 3.8) were categorised as pores by the algorithm, while the small holes (like in the bottom circle) were recognised as grains. This led to an incorrect pore perimeter/pore area ratio, therefore too high permeability values. Similarly to the previous sample, other parts of the picture with fewer irregularities were analysed, leading to lower porosity and permeability values.

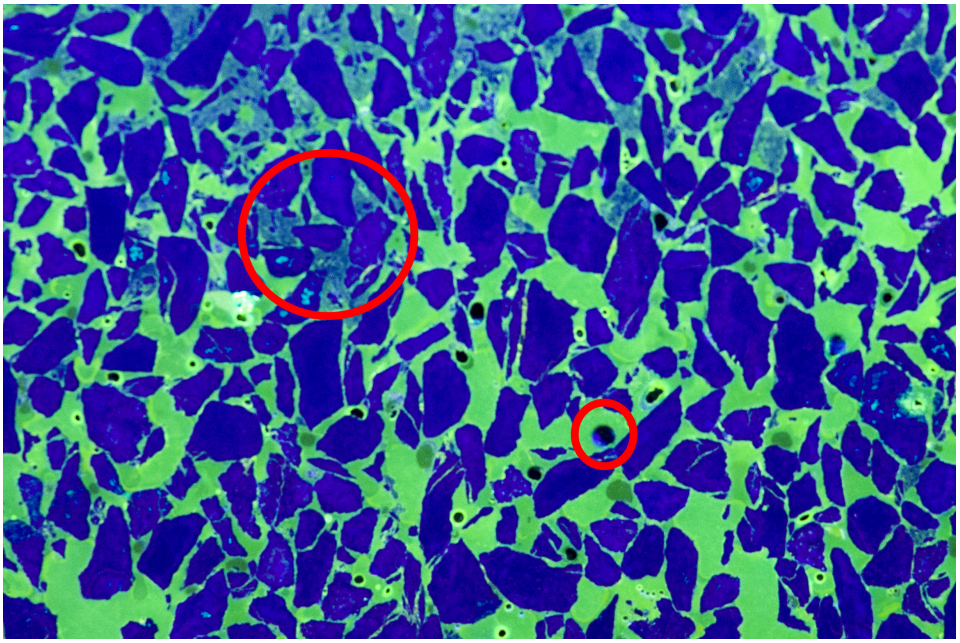

***Figure 3.8:*** *GPM37L with in red circles some irregularities contained in the sample.*

**GPM57 & GPM56** have grains covered by dye and large irregularities in parts of the samples. Cropping to different parts of the image again works to counteract the major heterogeneities. For the partially covered grains, darkening the blues (grains) with the black & white filter in Photoshop prevents the grains from being partially classified as pore space.

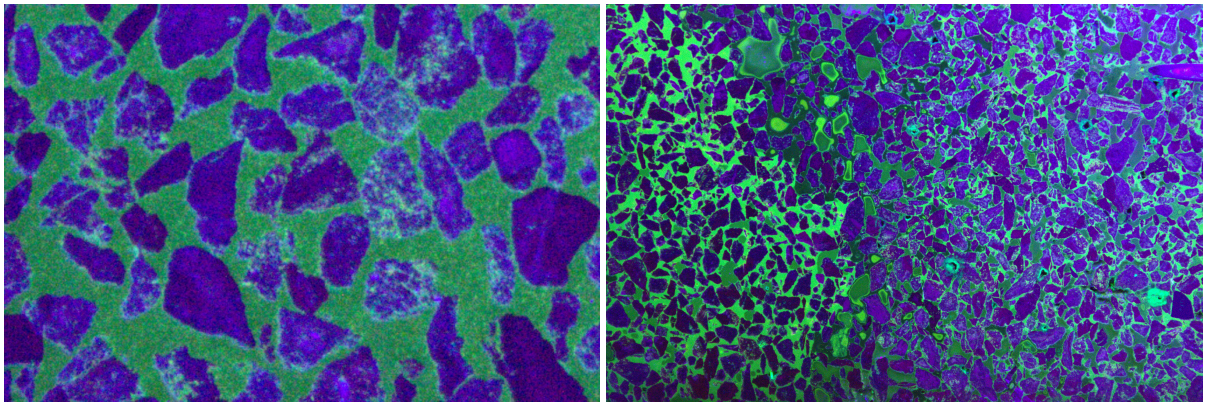

***Figure 3.9:*** *GPM56R (left), with grains covered by coating and GPM57R (right) with inconsistencies in the coating.*

After applying corrections to the samples, the final dataset was ready as seen in Appendix B. The maximum temperatures to which the samples were subjected were found in the PhD thesis of Wolf (2006) and these were plotted against the porosity and permeability as seen in Figure 3.10.

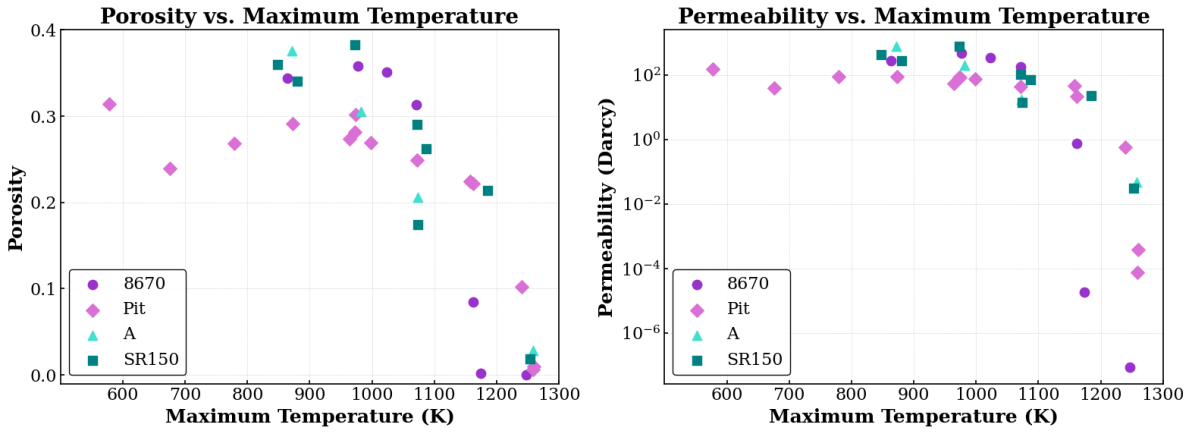


***Figure 3.10:*** *The relation between the temperature and the porosity and permeability of the samples.*

Looking at the graphs, both the porosity and permeability decrease as the temperature increases; this effect is especially noticeable from about 1100 K onwards. This can be explained by the melting point of many minerals that make up the samples being in the range of 900 - 1100 K, closing pores as they melt (Wang et al., 2023). The rate of decline is a lot higher for the permeability than for the porosity, as it is calculated using Equation 2.4, which contains a shape factor and the porosity with exponents. In Figure 3.11, the shape factor for all samples alongside the Kozeny-Carman dependence between porosity and permeability for fixed shape factors is shown.

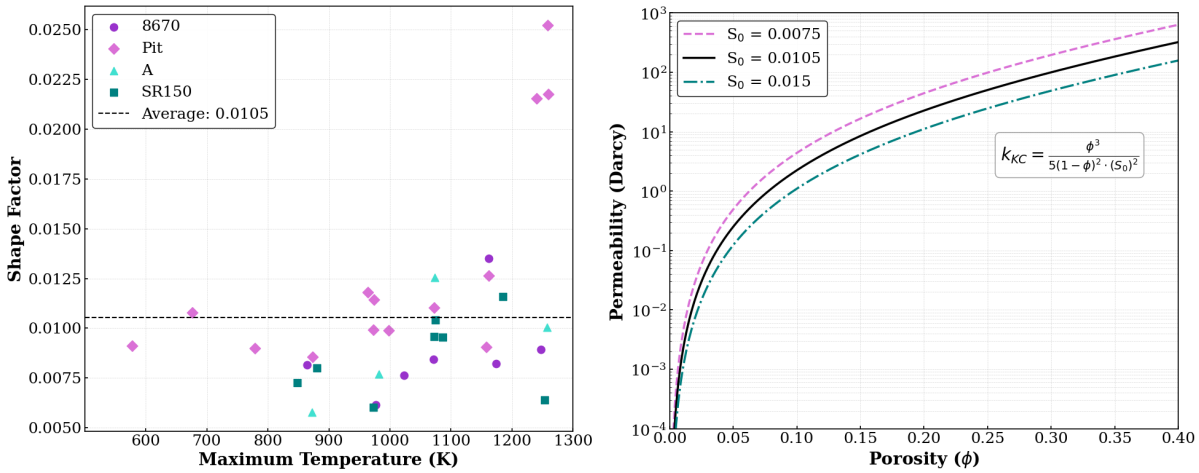


***Figure 3.11:*** *The relation between the temperature and shape factors for the samples (left) and the relation between porosity and permeability using Equation 2.4 for fixed shape factors (right).*

The graph on the left shows that there is no significant trend between the temperature and shape factors. Only the three Pit-series samples subjected to the highest temperatures have a shape factor that significantly exceeds the average (more than double). The rapid decrease in permeability at high temperatures can be attributed mostly to the porosity decrease, which is amplified by exponents in the KC-formula. As seen in the graph on the right, the rate of decline in permeability increases as the porosity decreases. A summary of the final porosity and permeability results can be found in Table 3.2, where for every three images of a sample, the standard deviation and coefficient of variation are calculated. These were then averaged for every sample series and overall.

Concerning the pressures, the copper tubes were subjected to annular pressures of 5 or 10 MPa. Due to the copper tube's yield stress, they behave elastically below a temperature of 900 K and visco-elastically above it. With the assumption that the samples are isotropic, the average stresses on the sample were calculated (Wolf, 2006) and presented in Appendix B.

***Table 3.2:*** *Mean values, standard deviations, and coefficients of variation (CV) of pictures for a sample averaged for all sample series.*

| **Sample Series** | **Porosity** | | | **Permeability (Darcy)** | | |
|---|---|---|---|---|---|---|
| | **Mean** | **Std. Dev.** | **CV** | **Mean** | **Std. Dev.** | **CV** |
| 8670-series | 0.208 | 0.022 | 10.5% | 202 | 98.9 | 48.8% |
| Pit-series | 0.218 | 0.026 | 12.0% | 60.5 | 36.1 | 59.8% |
| A-series | 0.229 | 0.021 | 9.3% | 257 | 131 | 51.0% |
| SR150-series | 0.255 | 0.022 | 8.6% | 218 | 66.2 | 30.4% |
| **Overall Average** | **0.226** | **0.023** | **10.1%** | **153** | **83.0** | **54.4%** |

The average standard deviation for the porosity is between 0.02 and 0.03 for all sample series, resulting in a CV of around 10%, which indicates that the results are stable and repeatable (Jalilibal et al., 2021). For the permeability, the CV is much higher, around 50%. This means that the outcomes of the permeability calculations for each of the 3 sample pictures differ from each other by a factor of 0.5 on average.

## 3.3. CT scanning results

The CT scans were performed for 3 samples: GPM63, GPM19, and GPM33. These were chosen because they all come from different series, have very different porosities and permeabilities from image analysis and show up differently under UV light. They were analysed in 3D for their porosity and permeability and in 2D for their porosities (for slices in the X, Y, and Z directions). These slices are shown in Figures 3.12, 3.13 and 3.14.

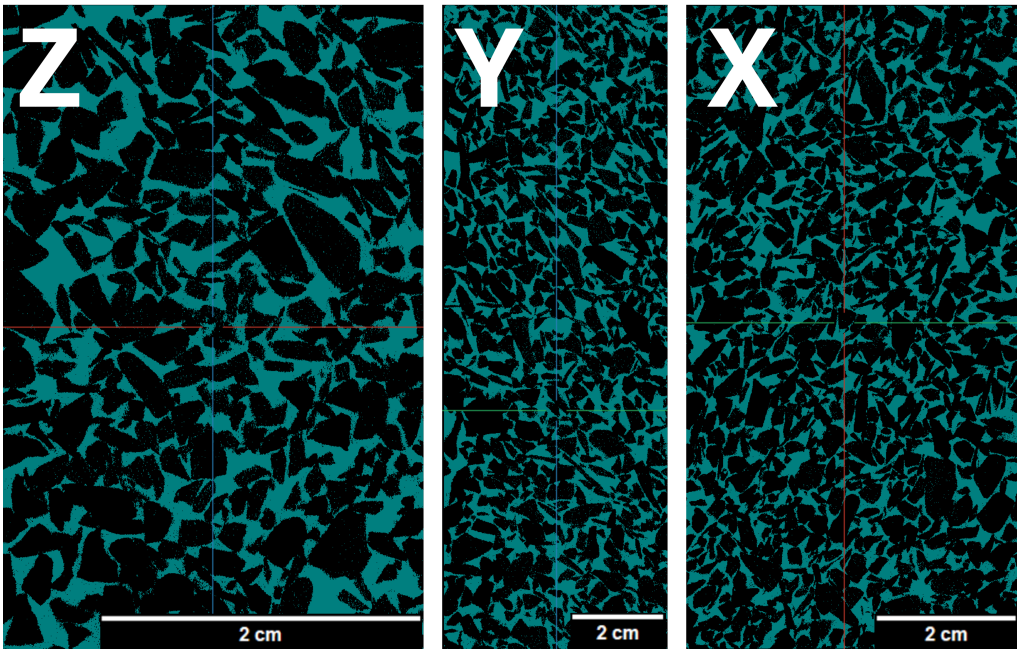


***Figure 3.12:*** *Three slices of GPM63, with the pores marked in blue and the grains in black.*

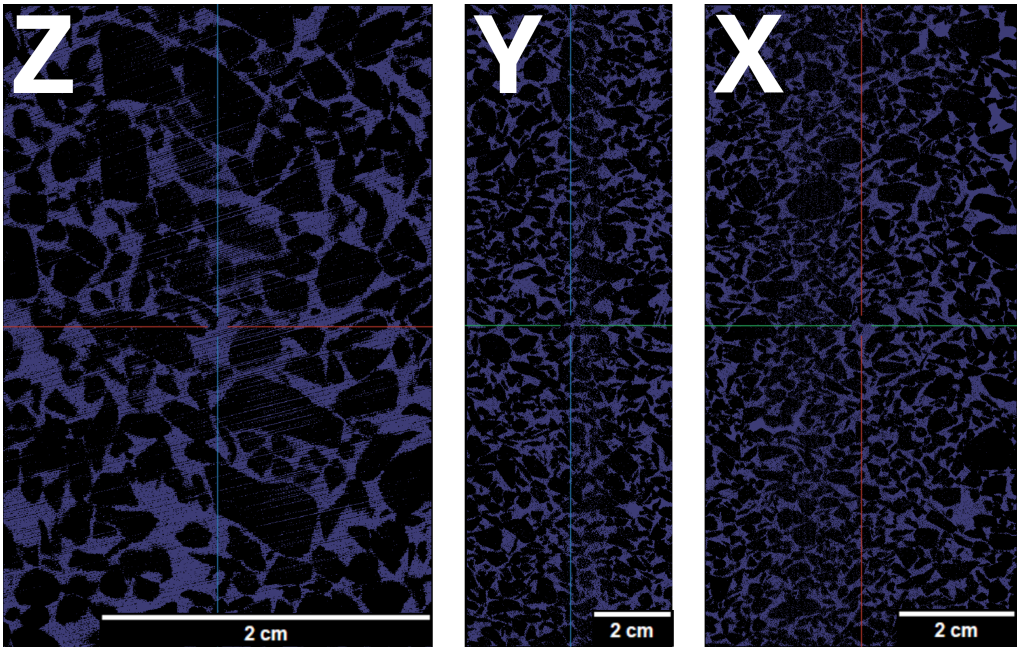


***Figure 3.13:*** *Three slices of GPM19, with the pores marked in purple and the grains in black.*

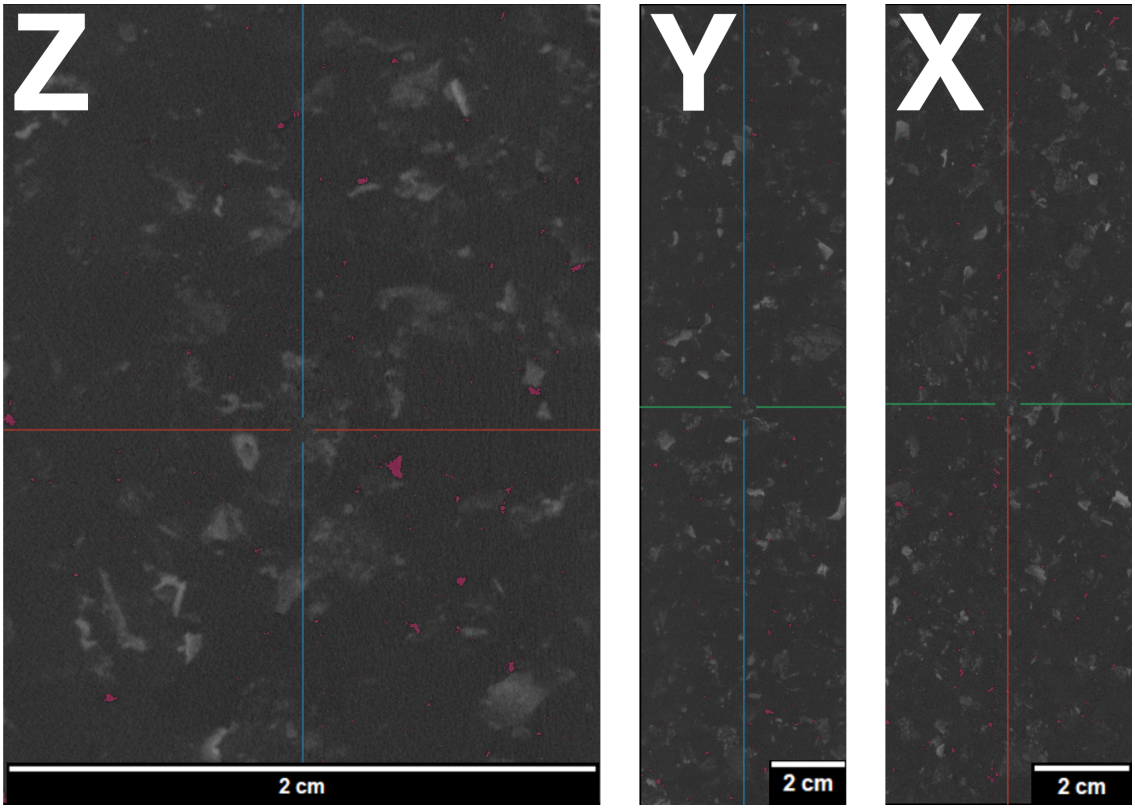


***Figure 3.14:*** *Three slices of GPM33, with the pores marked in pink. The light grey features are grains with a distinct colour.*

During the analysis of the slices, two issues were found. Samples GPM63 and GPM19 have a small hole in the bottom and sample GPM33 misses parts at the perimeter (Figure 3.15). Both of these increase the measured slice porosity, as it is calculated as the area of the pore space ROI divided by the total area.

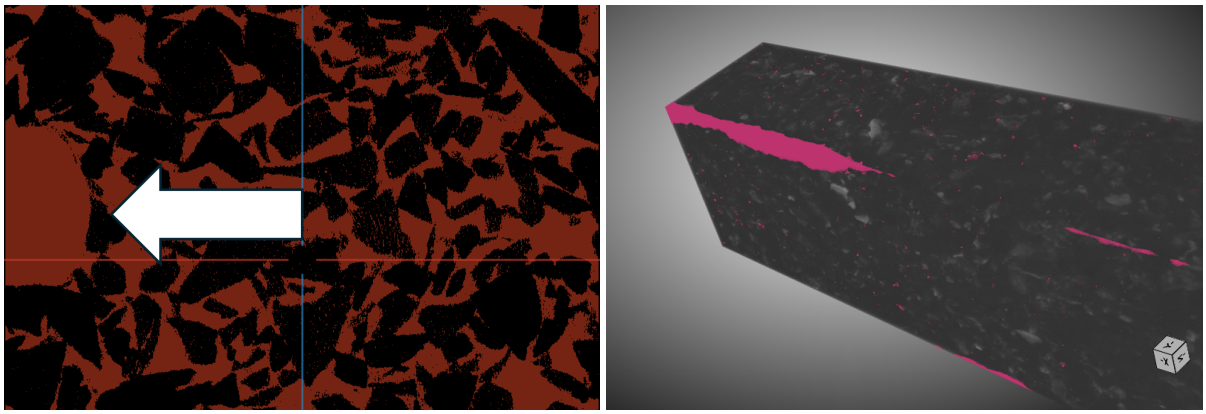

***Figure 3.15:*** *A slice of sample GPM63 with the hole (left) and a visualisation of GPM33 with missing parts (right).*

The porosity of all the analysed slices is plotted in Figures 3.16, 3.17 and 3.18. The shaded regions were affected by what was shown in Figure 3.15.

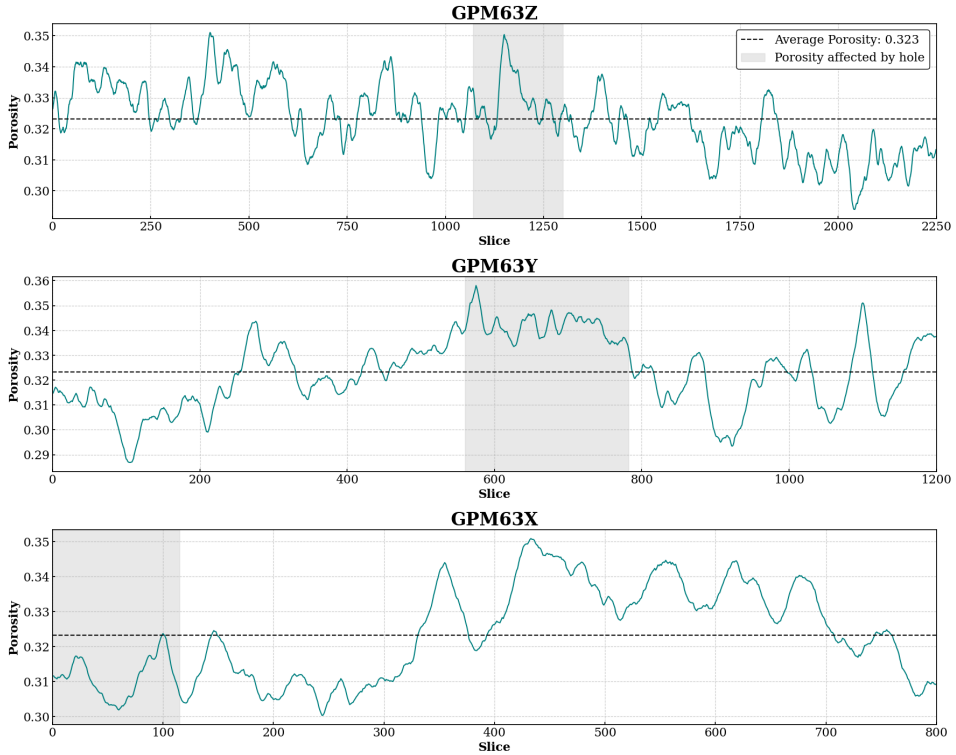


***Figure 3.16:*** *The porosity of 2D slices from CT-scanning of GPM63.*

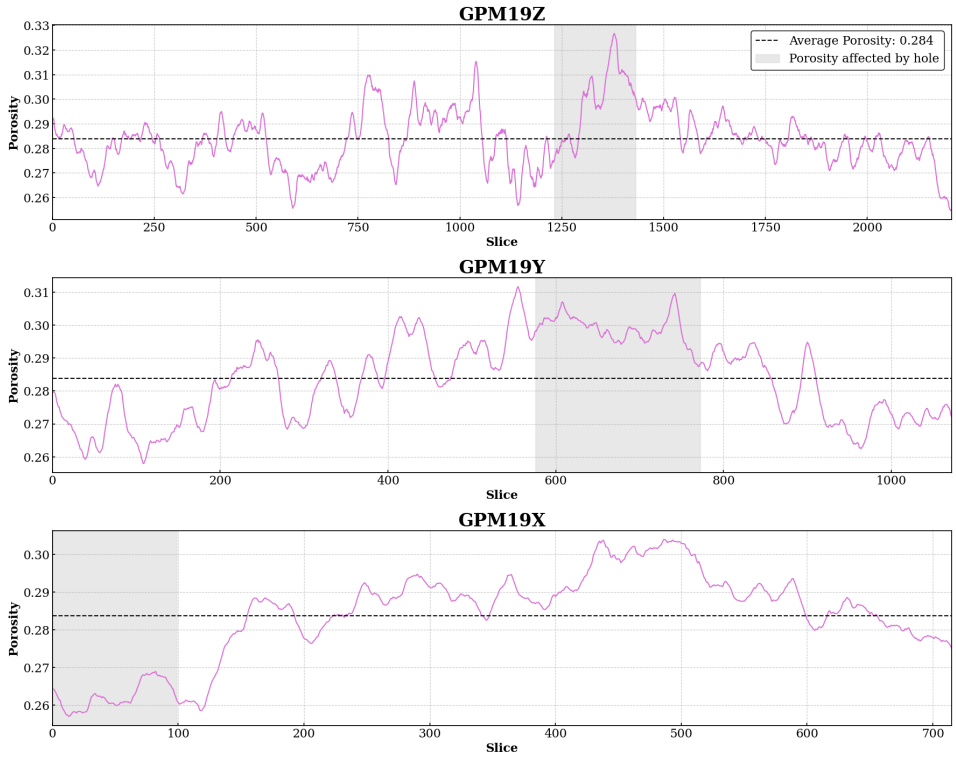


***Figure 3.17:*** *The porosity of 2D slices from CT-scanning of GPM19.*

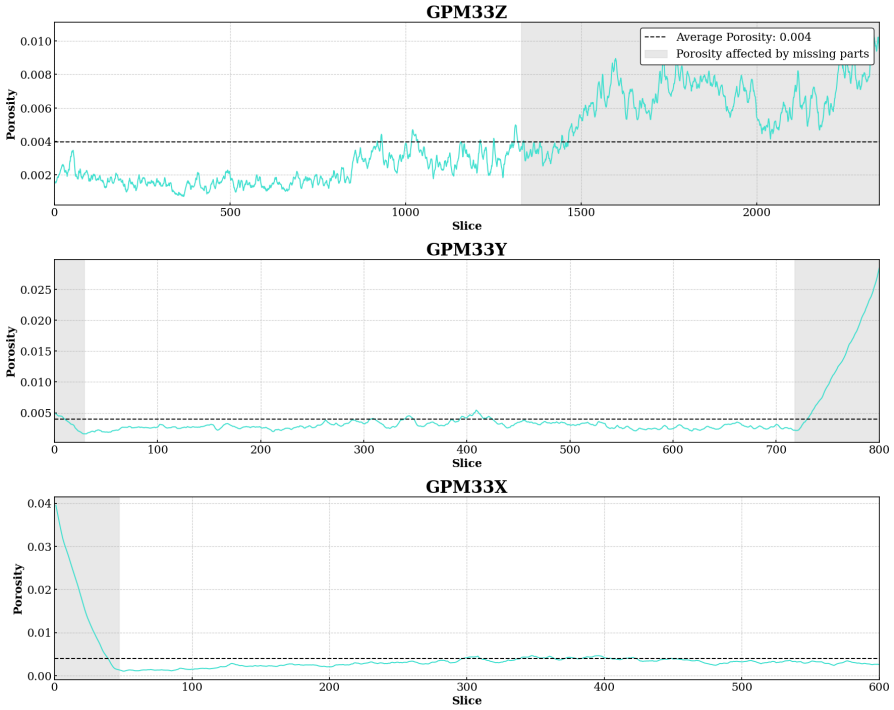


***Figure 3.18:*** *The porosity of 2D slices from CT-scanning of GPM33.*

For GPM63 and GPM19 the hole does not significantly increase the porosity. The porosity for the slices in the X direction for GPM63 is even lower than average. The missing parts of sample GPM33 have a large significance relatively speaking, but not in absolute values (except for the X direction again). To get the most accurate representation of the porosities of the samples, the results from the shaded areas were removed and histograms were plotted in Figure 3.19.

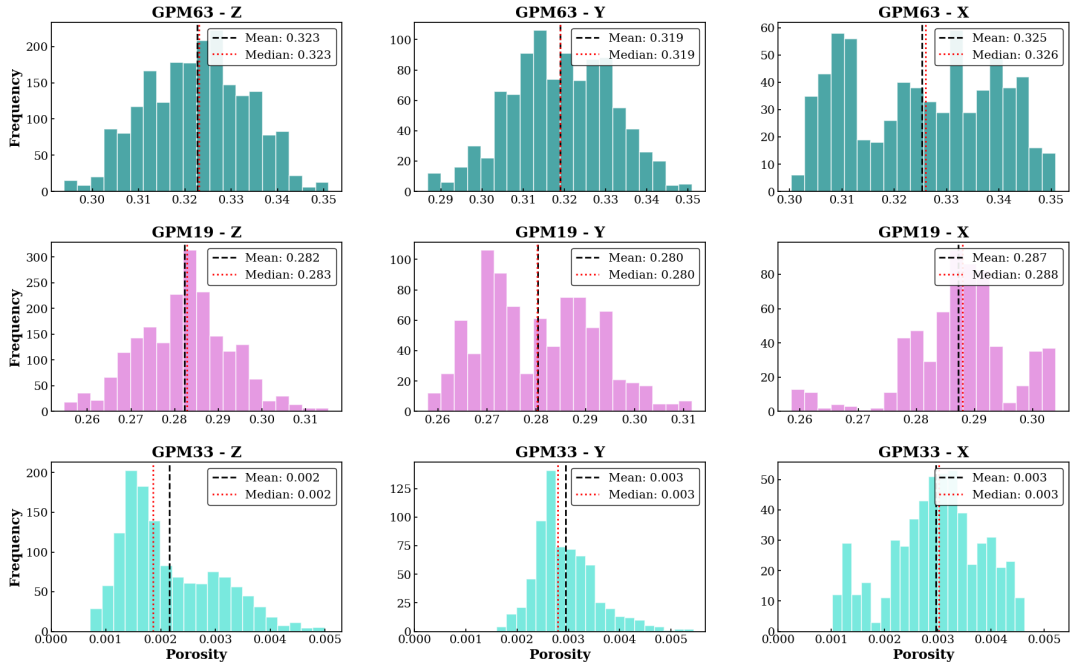


***Figure 3.19:*** *Histograms of the porosity of CT-scanned sample slices in three directions.*

The spread of porosity values is less than 0.03 for all samples in all directions, proving that the porosities are homogeneous throughout. With the slices that missed parts taken out, the porosities are on average a bit lower. Also, the porosities in the X, Y and Z directions now differ within the samples, since different slices were affected.

The three directions in which the slices were taken have an effect on the number of slices, their areas and therefore also the shape of the histograms in Figure 3.19. The slices in the Z direction have the smallest area and there are the most of them, as they are taken perpendicular to the longest dimension of the sample. For GPM63 and GPM19 their distributions resemble a bell curve, indicating that they are normally distributed. Sample GPM33 has a skewed distribution. An explanation for this is that about 40% of its slices had to be discarded, resulting in the slices with lower porosity, present in the first part of the sample, to be overrepresented. The Y direction cuts through the sample lengthwise, again perpendicular to the direction in which the photographs for image analysis were taken. Looking at the resulting histograms, GPM33 most closely resembles a normal distribution, with a spread of only 0.0035, indicating that the porosity is very homogeneous across these slices. The other two samples, especially GPM19, resemble a bimodal distribution. This is most likely a result of the grain rearrangement, as the grains repositioned themselves because of the high gas pressure introduced (Pressure Tubes (PT) in Figure 1.1, described by Wolf (2006)). By forming channels through which the gas can flow, a cluster of more porous and less porous slices is formed. This same effect can be observed in the X direction for all the samples.

These porosity histograms can be translated into permeability histograms using Equation 2.2. Since the shape factor cannot be easily computed for every slice of every sample and since Figure 3.10 shows that the influence of porosity on permeability is much greater than the effect of the shape factor, it was decided to use the average shape factor from image analysis, 0.0105.

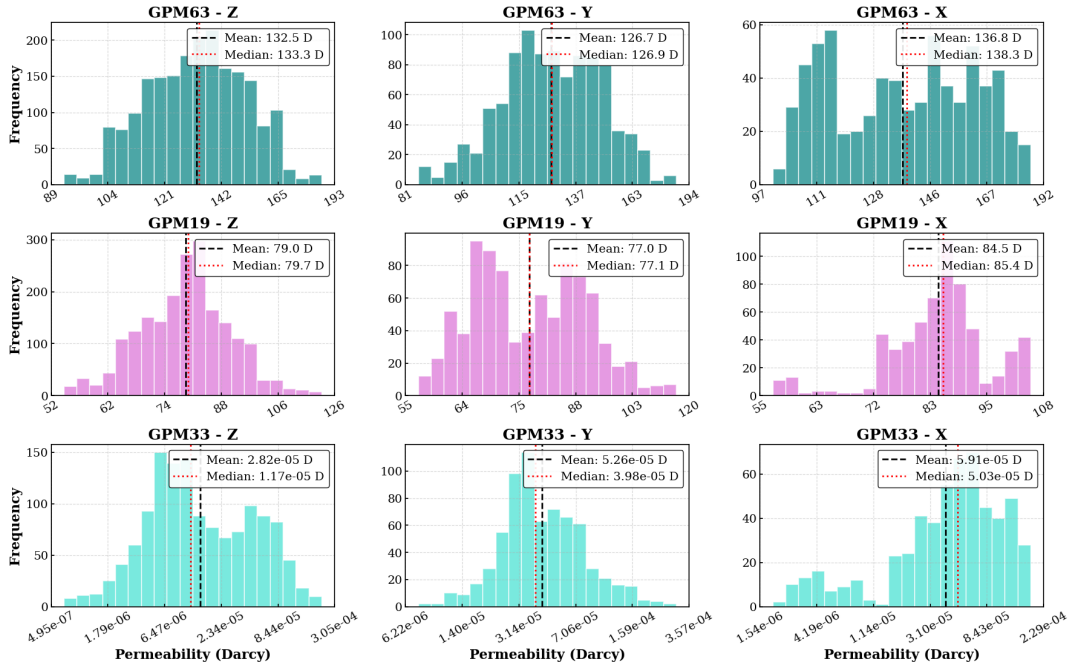


***Figure 3.20:*** *Histograms of the permeability of CT-scanned sample slices in three directions. The average shape factor of 0.0105 was used for the calculations.*

Similar trends to those from the porosity histograms are observed in the permeability histograms in Figure 3.19. What is most interesting here is to compare the average permeability values to those calculated for the entire 3D structure using Equation 2.7. Table 3.3 lists the CT scanning results for the porosity and permeability, both from direct 3D calculations and the average of the slices. For the porosity the difference is small and caused only by the fact that for the slice calculations, the slices containing *faulty* regions were removed. The permeability difference is bigger: for GPM63 the average slice porosity is roughly triple, for GPM19 it is about 6.5 times larger and for GPM33 it differs by 2 orders of magnitude. This is mainly because a fixed shape factor, taken from image analysis, is used for the slice calculations, instead of using the modified shape factor from Equation 2.7.

***Table 3.3:*** *CT scanning results.*

| **Sample** | **Porosity** | | **Permeability (Darcy)** | |
|---|---|---|---|---|
| | **3D** | **Avg. 2D Slice** | **3D** | **Avg. 2D Slice** |
| GPM63 | 0.323 | 0.322 | 47.1 | 132.0 |
| GPM19 | 0.284 | 0.283 | 12.0 | 80.1 |
| GPM33 | 0.004 | 0.003 | $6.7 \times 10^{-7}$ | $4.7 \times 10^{-5}$ |

# 4 Discussion

A validation of the results will be performed by considering the limitations of image analysis and CT scanning for the calculation of the porosity and permeability. After this, the data will be compared to the work done by Wolf (2006) on the same samples and to other papers discussing the effect of high temperatures and pressures on the porosity and permeability. This is followed by a section comparing the 2D and 3D results, discussing the differences, benefits and drawbacks of either method. The discussion ends with the implications of this research and a highlight of the further research opportunities.

## 4.1. Validity of Results

Many factors influence the image analysis results, with every step adding another level of uncertainty. This starts with the quality of the sample itself and the impregnation with epoxy, which varies widely and poses a challenge when photographing, as described in section 3.1. Another influencing factor described in the same section is the type of light used to photograph the samples. Although neither of these can be quantified directly, they do impact the quality of the raw images. What can be quantified is the uncertainty of the thresholding technique, where in section 2.6 the CT scan porosity with the Otsu method deviates from manual thresholding by more than 0.9 for one of the samples, confirming that Otsu is not suitable for this dataset. This large deviation justified the (also undesired) use of manual thresholding instead.

This highlights an advantage of 2D image analysis over CT scanning: the ability to change the lighting settings and set the greyscale threshold based on colours from the image removes the need for manual thresholding. To limit the uncertainty in the processing steps, all samples were processed using the same methodology, except for some tweaking with the black & white filter settings, as this was unavoidable in some cases. Even so, whenever the settings were changed, it was only done by setting the value of ”blue” to the minimum, therefore not introducing further human biases.

Assuming that there are no systematic measurement errors, the image analysis and CT scanning results can be used to identify that for high temperatures (at least above 1100 K), both the porosity and permeability decrease. This is evidenced by the consistent trend and these results being in line with previous findings by G. Wu et al. (2013). The porosity values from image analysis have a low coefficient of variation and can therefore also be used to estimate the exact sample porosity, especially when taking the average of multiple pictures. The permeability calculations, on the other hand, with CVs around 50% and standard deviations ranging from tens to over a hundred Darcy, are not precise enough to determine absolute values.

No clear trend could be found between the pressure and the porosity/permeability, because there are no samples with the same temperature, where only the pressure varies. The pressure is needed to compact the grains, as just the temperature would not be able to do that.

## 4.2. Comparison to Previous Work

The samples used in this thesis were originally prepared and analysed for the doctoral thesis by Wolf (2006). The results from this can be directly compared to the new image analysis results to see if the same values and trends are found.

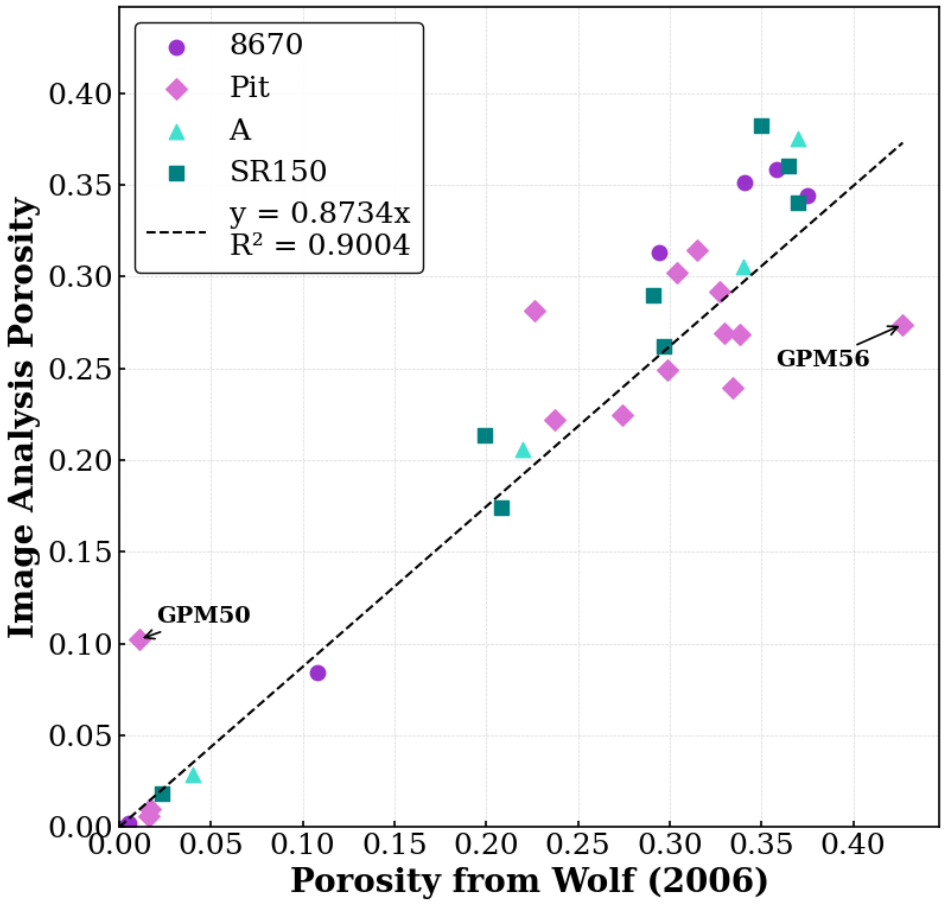


***Figure 4.1:*** *A comparison of the new image porosity and the image porosity from Wolf (2006).*

As can be seen, the porosities are in good accordance with each other with an $R^2$ value of 0.90. The best linear trend line, $y = 0.87x$, is a bit below the line $y = x$, mainly because of some samples from the Pit-series. Most samples are very close to the line $y = x$, which means that the new measurements are in agreement with the original measurements. There are 2 notable outliers: GPM50, where the new porosity is higher than the original and GPM56, where the new porosity is lower than the original. Both of these samples have some grains covered by dye (see Figure 3.9 for GPM56), which is the most probable cause for the differences in image processing results.

The same can be done for the permeability, plotted on a logarithmic scale because of the wide range of values.

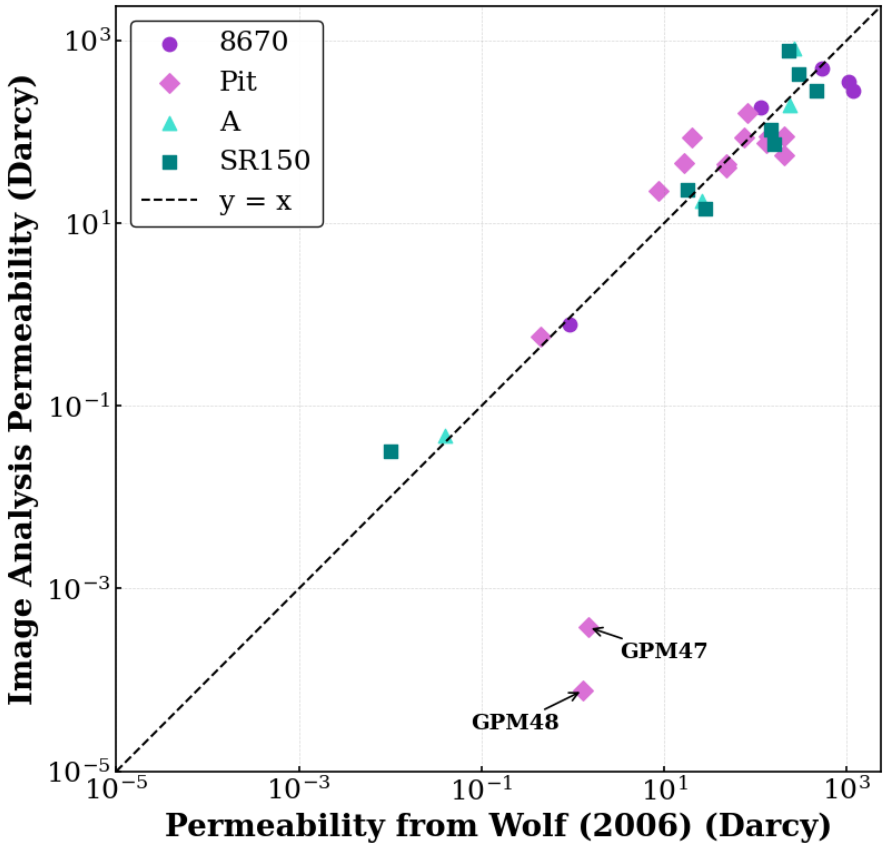


***Figure 4.2:*** *A comparison of the new image permeability and the image permeability from Wolf (2006).*

Again, many of the results line up, as can be seen by how close they are to the line $y = x$. The log-scale can make the values seem closer than they really are though, all exact values can be found in Appendix B. The biggest outliers are GPM48 and GPM47. The reason for this can be seen from the graph, namely the fact that the permeability is so low. The images of these samples have very few and small pores, which amplifies the effects of errors and open cycles, in which many grains can get fully eroded away (Said and Jambek, 2021). The permeability calculation (Equation 2.4) leads to an overrepresentation of these small pores, which do not influence the permeability as much according to Luo et al. (2024). The permeability results of samples like these should therefore be considered with reservations.

Besides a direct comparison using the same samples, the results are also compared to the papers by Zhang et al. (2021) and G. Wu et al. (2013), both of which describe the effects of high temperatures on the porosity of rocks. They both mention an increase in porosity due to the formation of cracks from a temperature of 700-800 K. This was not observed here, which is because rubble samples were used as opposed to rocks. Under the higher pressures and temperatures, the grains could easily rearrange, whereas in a rock, cracks would form. What was observed is a rapid decrease in porosity and permeability from a temperature of about 1100 K. The same is described by G. Wu et al. (2013) in their laboratory experiments. They attribute this to the melting of minerals inside of the rocks, which then go on to fill the pores. Zhang et al. (2021) also found a decrease, but only from a temperature of around 1300 K. This study, however, was performed on red sandstone, which contains more quartz and hematite (both of which have a high melting point) than the samples collected by Wolf (2006).

## 4.3. A Comparison of 2D and 3D Methods

Since the three samples that were analysed with the CT scanner have also been analysed using image analysis, their methodologies and results can be compared and discussed. It was already highlighted in section 4.1 that the 2D image analysis has an advantage over the 3D CT scanning because it captures colours, not only brightnesses. Another advantage of image analysis is that it has a higher resolution, meaning more pixels and potentially more of the small pores being captured. The camera takes pictures with a resolution of 800 pixels per cm, meaning pixel dimensions of 12.5 $\mu$m. The CT scans have voxel (3D pixel) dimensions of 25 $\mu$m, meaning the resolution is twice as bad. To investigate the influence of the resolution, the pictures used for image analysis were compressed using Photoshop to have the same resolution as the CT scans. Table 4.1 contains the porosity and permeability results for the original photographs, the compressed ones and CT scanning.

***Table 4.1:*** *A comparison between the porosity and permeability from image analysis (IA), CT scanning and compressed IA (with the same resolution as the CT scans).*

| **Sample** | **Porosity** | | | **Permeability (Darcy)** | | |
|---|---|---|---|---|---|---|
| | **IA** | **IA Compressed** | **CT** | **IA** | **IA Compressed** | **CT** |
| GPM63 | 0.351 | 0.355 | 0.322 | 354 | 382 | 47.1 |
| GPM19 | 0.290 | 0.291 | 0.284 | 106 | 110 | 12.0 |
| GPM33 | 0.028 | 0.024 | 0.004 | 0.047 | 0.009 | $6.7E{-}07$ |

The porosity results for the compressed images deviate by less than 0.01 from the original ones and the permeabilities differ by at most 28 Darcy. For samples GPM63 and GPM19, the compressed images yield higher porosity and permeability results, while CT scanning produces lower results. The image resolution can therefore not be the cause of the discrepancy between image analysis and CT scanning. For sample GPM33, the porosity and permeability results **are** lower for the compressed sample. This is because GPM33, unlike the other 2 samples, is dominated by very small pores, which can disappear in the compression process; the averaging of the pixels may lead them to become part of the grain pixels. For the samples which are dominated by larger pores, the effect of the compression is that the pore/grain boundaries get smoothed (Ungureanu, Negirla, and Korodi, 2024), resulting in a net slightly higher porosity and a smaller shape factor (due to a shorter pore perimeter) thus a higher permeability as well.

The porosity differences between the original image analysis results and CT scanning are within 0.03 in absolute values. Relatively speaking, the differences in porosity values for GPM63 and GPM19 are within 10%, while for GPM33 the value from the CT scan is 7 times lower. This can again be explained by the porosity being very low for that sample, which amplifies slight porosity deviations (the porosity of the exposed surface might be far above the average). While it was expected that CT scanning would be preferred due to its ability to uncover the 3D pore structure, the lower contrast between grains and pores compared to the image analysis, resulting from the lack of pixel colour data, meant that thresholding had to be done manually, reducing the reliability of the results. This confirms that even with all the advances in imaging technology, computer software still struggles to segment geological features which can easily be distinguished by the human eye, requiring image modification or software training to solve (Brondolo and Beaussant, 2025; Russ, 1986).

Comparing the permeabilities in Table 4.1, there is a significant difference between the results for all samples. Three possible reasons for this were identified:

1. There are flaws in the way Dragonfly was used to calculate the permeability.
2. One or both of the KC-calculations are not a valid method of calculating the permeability.
3. 2D image analysis is substantially better or worse than 3D CT scanning for permeability measurements.

The first reason is the most likely. Firstly, the 3D results presented here already deviate substantially from the average of the slices calculated with the shape factor from image analysis as shown in Table 3.3. This still does not explain it fully, because the average of the CT slice permeabilities is at best, for sample GPM63, a factor of 3 smaller from the image analysis permeability. The second reason is partly valid, as there are limitations to the accuracy of permeability calculations using the Kozeny-Carman relationship as described by Yin et al. (2022), Marshall (1957), and Wolf (2006). It is, however, still widely used and adopted, as it provides a good estimate (Yin et al., 2022). Moreover, the same formula was used for both methods. Then the third reason. As previously mentioned, the resolution of the digital camera used for image analysis is double that of the CT scanner. Moreover, the CT scans do not capture colour data, which is helpful in thresholding, especially when a highly contrasting dye is used to distinguish between the pores and grains. So, CT scanning, despite being able to quantify the samples in 3D, is less suitable than traditional 2D image analysis for the determination of the porosity and permeability of these samples.

## 4.4. Further Research

The main difficulty during this thesis was dealing with the differences in impregnation quality. Not only did this mean that some samples were challenging to analyse, but it also meant that the camera and lighting had to be continuously adjusted. A recommendation for further research would therefore be to look into the creation of the samples again and into how the coating and impregnation process can be improved.

Regarding the CT scanning, the results were not satisfactory. A method should be found to improve the segmentation process, eliminating the need for manual thresholding. Furthermore, running a permeability simulation on the data from the CT scan would validate the image analysis results in a way that a calculated 3D permeability cannot.

# 5 Conclusion

This report aimed to delve into how image analysis can be used to measure the porosity and permeability of rock samples subjected to high temperatures and pressures. The analysed samples originated from the doctoral research by Wolf (2006), subdivided into four sample series based on their origin and composition. The following actions were performed:

- The samples were sorted and photographed using both UV and normal light, depending on which is more suitable.
- The images were processed and segmented using Photoshop and ImageJ. The porosities and permeabilities were visualised graphically using Python.
- Three samples were selected and scanned using a micro-CT scanner. The scans were processed using Dragonfly 3D and the results were compared to the image analysis results. Additionally, the individual slices were analysed and *faulty* slices were removed.

The following conclusions were drawn:

- If a sample is properly impregnated with a fluorescing dye, then the image analysis will work better with a UV light source; if it is not, then the results may vary.
- As the maximum temperature that a rock sample has been subjected to increases, the porosity and permeability of that sample decrease. No clear trend was found for the pressure, although it must be present in order for the compaction to take place.
- The porosity and permeability trends obtained from image analysis are in agreement with the results from Wolf (2006). The exact values do not always line up well, particularly for low permeabilities.
- The porosities from image analysis are in agreement with those from CT scanning. The calculated permeabilities from CT scanning are consistently lower.
- 3D methods do not always lead to better results than 2D methods. A lot depends on the processing. The higher resolution and presence of colour data for regular imaging mean that it was the preferred method for these samples.

This report was able to show how modern imaging equipment can be used for the analysis of porous rock samples. Regardless of the issues with the quality of the samples, the image analysis results were of good quality and their results could be used to validate previous research on these samples. For future research, it is recommended to explore CT processing further, especially regarding permeability simulations as well as optimising epoxy creation and impregnation techniques.

# References


Ache, Benjamin (Mar. 2022). *What is Micro-CT? an introduction*. URL: https://www.microphotonics.com/what-is-micro-ct-an-introduction/.

Al Marzouqi, Hasan (Mar. 2018). "Digital Rock Physics: Using CT Scans to Compute Rock Properties". In: *IEEE Signal Processing Magazine* 35, pp. 121–131. DOI: 10.1109/MSP.2017.2784459.

Alberts, Luc J.H. (2005). *Initial Porosity of Random Packing: Computer simulation of grain rearrangement*. Department of Geotechnology, Delft University of Technology.

Aqui, A.R. and S. Zarrouk (Nov. 2011). "Permeability Enhancement of Conventional Geothermal Wells". In: *Proceedings of the New Zealand Geothermal Workshop 2011*. University of Auckland. Auckland, New Zealand.

Bangare, Sunil et al. (May 2015). "Reviewing Otsu's Method For Image Thresholding". In: *International Journal of Applied Engineering Research* 10, pp. 21777–21783. DOI: 10.37622/IJAER/10.9.2015.21777-21783.

Belcher, Claire M., ed. (2013). *Fire Phenomena and the Earth System: An Interdisciplinary Guide to Fire Science*. Chichester, UK: John Wiley & Sons. ISBN: 978-1-118-52956-0.

Brondolo, Florent and Samuel Beaussant (2025). "DINOv2 rocks geological image analysis: Classification, segmentation, and interpretability". In: *Journal of Rock Mechanics and Geotechnical Engineering*. ISSN: 1674-7755. DOI: 10.1016/j.jrmge.2025.01.057. URL: https://www.sciencedirect.com/science/article/pii/S1674775525002677.

Comet Technologies Canada Inc. (2024). *Porous Microstructure Analysis (PUMA)*. URL: https://www.theobjects.com/dragonfly/dfhelp/2024-1/Content/Extending%20Dragonfly/Porous%20Microstructure%20Analysis%20(PuMA)/Porous%20Microstructure%20Analysis%20(PuMA).htm.

Datta, Debabrata et al. (2015). "An Image Analysis Technique to Estimate the Porosity of Rock Samples". In: *IJSRD - International Journal for Scientific Research & Development* 3.10. Available at: https://www.ijsrd.com/Article.php?manuscript=IJSRDV3I100214, pp. 835–838. ISSN: 2321-0613.

Hassanzadegan, Alireza et al. (Mar. 2014). "The Effects of Temperature and Pressure on the Porosity Evolution of Flechtinger Sandstone". In: *Rock Mechanics and Rock Engineering* 47.2, pp. 421–434. ISSN: 1434-453X. DOI: 10.1007/s00603-013-0401-z. URL: https://doi.org/10.1007/s00603-013-0401-z.

Hettema, M.H.H. (1996). "The thermo-mechanical behaviour of sedimentary rock". In: URL: https://resolver.tudelft.nl/uuid:8f733adc-9765-4005-94e8-84d190295cf1.

Jaber, H. et al. (2024). "The effect of temperature on the mechanical and hydraulic properties of sedimentary rocks". In: *Geoenergy Science and Engineering* 235, p. 212702. ISSN: 2949-8910. DOI: https://doi.org/10.1016/j.geoen.2024.212702. URL: https://www.sciencedirect.com/science/article/pii/S2949891024000721.

Jalilibal, Zahra et al. (2021). "Monitoring the coefficient of variation: A literature review". In: *Computers & Industrial Engineering* 161, p. 107600. ISSN: 0360-8352. DOI: 10.1016/j.cie.2021.107600. URL: https://www.sciencedirect.com/science/article/pii/S0360835221005040.

Luo, Yinwei et al. (Dec. 2024). "Quantitative analysis of pore-size influence on granite residual soil permeability using CT scanning". In: *Journal of Hydrology* 645, p. 132133. ISSN: 0022-1694. DOI: 10.1016/J.JHYDROL.2024.132133.

Mandarim-de-Lacerda, Carlos, Caroline Fernandes-Santos, and Marcia Aguila (Jan. 2010). "Image Analysis and Quantitative Morphology". In: *Methods in molecular biology (Clifton, N.J.)* 611, pp. 211–225. ISSN: 978-1-60327-344-2. DOI: 10.1007/978-1-60327-345-9_17.

Marshall, T J (1957). "Permeability and the Size Distribution of Pores". In: *Nature* 180 (4587), pp. 664–665. ISSN: 1476-4687. DOI: 10.1038/180664a0. URL: https://doi.org/10.1038/180664a0.

Oberholzer, Martin et al. (1996). "Methods in quantitative image analysis". In: *Histochemistry and Cell Biology* 105 (5), pp. 333–355. ISSN: 1432-119X. DOI: 10.1007/BF01463655. URL: https://doi.org/10.1007/BF01463655.

OSREM (2025). *Coal Mine Fires and Burning Refuse*. http://www.osmre.gov/programs/mine-fires. Accessed June 29, 2025.

Panda, Manmath and Larry Lake (July 1994). "Estimation of Single-Phase Permeability from Parameters of Particle-Size Distribution". In: *Aapg Bulletin - AAPG BULL* 78, pp. 1028–1039.

Russ, John C (Sept. 1986). *Practical Stereology*. 1986th ed. Kluwer Academic/Plenum.

Said, K and Asral Jambek (Oct. 2021). "Analysis of Image Processing Using Morphological Erosion and Dilation". In: *Journal of Physics: Conference Series* 2071, p. 012033. DOI: 10.1088/1742-6596/2071/1/012033.

Schindelin, Johannes et al. (2012). "Fiji: an open-source platform for biological-image analysis". In: *Nature Methods* 9.7, pp. 676–682. DOI: 10.1038/nmeth.2019.

ScienceDirect (n.d.). *Porosity Measurement - an overview | ScienceDirect Topics*. https://www.sciencedirect.com/topics/engineering/porosity-measurement. Accessed: 2025-06-30.

Serra, Jean (1982). *Image analysis and mathematical morphology*. Trans. by Noel A.C. Cressie. Academic Press.

SLB (2025). *permeability | Energy Glossary*. [Online; accessed 2025-03-20]. URL: https://glossary.slb.com/en/Terms/p/permeability.aspx.

Smith, Steven W. (1997). "Chapter 25: Special Imaging Techniques". In: *The Scientist & Engineer's Guide to Digital Signal Processing*. 1st ed. California Technical Publishing.

Sparavigna, Amelia Carolina (Jan. 2020). "On the Use of ImageJ Segmentation". In: DOI: 10.5281/zenodo.3629411.

Šperl, Jan and Jiřina Trčková (2008). "Permeability and Porosity of Rocks and Their Relationship Based on Laboratory Testing". In: *Acta Geodynamica et Geomaterialia* 5.1 (149). Received October 2007, accepted January 2008, pp. 41–47. ISSN: 1214-9705.

Underwood, Ervin E. (1970). *Quantitative Stereology*. Addison-Wesley.

Ungureanu, Vlad-Ilie, Paul Negirla, and Adrian Korodi (2024). "Image-Compression Techniques: Classical and "Region-of-Interest-Based" Approaches Presented in Recent Papers". In: *Sensors* 24.3. ISSN: 1424-8220. URL: https://www.mdpi.com/1424-8220/24/3/791.

Wang, Tao et al. (2023). "Research progress and visualization of underground coal fire detection methods". In: *Environmental Science and Pollution Research* 30 (30), pp. 74671–74690. ISSN: 1614-7499. DOI: 10.1007/s11356-023-27678-8. URL: https://doi.org/10.1007/s11356-023-27678-8.

Wolf, Karl-Heinz A.A. (2006). "The interaction between underground coal fires and their roof rocks". In: URL: https://resolver.tudelft.nl/uuid:dd06906f-9172-43a6-ac5a-5849bda1ddc1.

Wu, G. et al. (Apr. 2013). "Laboratory Investigation of the Effects of Temperature on the Mechanical Properties of Sandstone". In: *Geotechnical and Geological Engineering* 31.2, pp. 809–

816. ISSN: 1573-1529. DOI: 10.1007/s10706-013-9614-x. URL: https://doi.org/10.1007/s10706-013-9614-x.

Wu, Jian Jun and Xiao chen Liu (Apr. 2011). "Risk assessment of underground coal fire development at regional scale". In: *International Journal of Coal Geology* 86 (1), pp. 87–94. ISSN: 0166-5162. DOI: 10.1016/J.COAL.2010.12.007.

Yin, Peijie et al. (2022). "The Modification of the Kozeny–Carman Equation through the Lattice Boltzmann Simulation and Experimental Verification". In: *Journal of Hydrology* 609, p. 127738. ISSN: 0022-1694. DOI: 10.1016/j.jhydrol.2022.127738. URL: https://www.sciencedirect.com/science/article/pii/S0022169422003134.

Yu, Wonpil (2004). "Practical anti-vignetting methods for digital cameras". In: *IEEE Transactions on Consumer Electronics* 50 (4), pp. 975–983. ISSN: 1558-4127. DOI: 10.1109/TCE.2004.1362487.

Zhang, He et al. (Feb. 2021). "Effects of high-temperature thermal treatment on the porosity of red sandstone: an NMR analysis". In: *Acta Geophysica* 69.1, pp. 113–124. ISSN: 1895-7455. DOI: 10.1007/s11600-020-00526-w. URL: https://doi.org/10.1007/s11600-020-00526-w.

# A Python code

**Code for calculating the porosity and permeability from a .csv file containing the grain areas and perimeters.**

```
import numpy as np
import pandas as pd

# FILL IN FOR EVERY SAMPLE
#################################
data = pd.read_csv('Sample_filename.csv')
height = 2 # in cm
width = 3 # in cm
#################################

total_area = height*width # in cm^2

def calc_porosity(data, total_area):
    pore_area = np.sum(data['Area']) # in cm^2
    porosity = pore_area/total_area # unitless
    return porosity, pore_area

porosity = calc_porosity(data, total_area)[0]
pore_area = calc_porosity(data, total_area)[1]

def calc_permeability(data, porosity, pore_area):
    pore_perimeter = np.sum(data['Perim.']) # in cm
    permeability = porosity**3/(5 * (1-porosity)**2*((4/np.pi) * (
        pore_perimeter/pore_area))**2) # in cm^2
    permeability = permeability * 1e-4 * 1.01324997e+12 #Convert to Darcy
    # print('PpAp_avg:', pore_perimeter/pore_area)
    return permeability

# Print results
file_name = data['Label'][1]
file_name = file_name[:-4]
print('Sample:', file_name)
print('Porosity: {:.3f}'.format(porosity))
print('Permeability: {:.0f}'.format(calc_permeability(data, porosity,
    pore_area)), 'Darcy')
```

# B Sample Data

***Table B.1:*** *An overview of the results for all samples.*

| Sample | Porosity | Permeability | Max. Temperature | Max. Pressure | Values from Wolf (2006) | |
|---|---|---|---|---|---|---|
| | (-) | (Darcy) | (K) | (MPa) | **Porosity** | **Permeability** |
| **8670-series** | | | | | | |
| GPM61 | 0.344 | 283.94 | 864.0 | 10.0 | 0.375 | 1188.47 |
| GPM54 | 0.358 | 492.15 | 977.0 | 5.0 | 0.358 | 535.31 |
| GPM63† | 0.351 | 354.31 | 1023.0 | 10.0 | 0.341 | 1062.89 |
| GPM53 | 0.313 | 183.00 | 1071.0 | 5.0 | 0.294 | 116.01 |
| GPM52 | 0.084 | 0.78 | 1162.0 | 5.0 | 0.108 | 0.91 |
| GPM62 | 0.0018 | $1.9 \times 10^{-5}$ | 1174.0 | 10.0 | 0.005 | 0.00 |
| GPM51 | 0.0003 | $8 \times 10^{-8}$ | 1247.0 | 5.0 | 0.003 | 0.00 |
| **Pit-series** | | | | | | |
| GPM60 | 0.314 | 158.87 | 578.0 | 10.0 | 0.315 | 83.08 |
| GPM59 | 0.239 | 40.60 | 676.0 | 10.0 | 0.334 | 47.95 |
| GPM58 | 0.269 | 89.47 | 779.0 | 10.0 | 0.338 | 138.04 |
| GPM57 | 0.292 | 90.50 | 873.0 | 10.0 | 0.327 | 208.36 |
| GPM56 | 0.274 | 54.83 | 964.0 | 10.0 | 0.427 | 206.75 |
| GPM55 | 0.281 | 87.72 | 973.0 | 10.0 | 0.226 | 20.35 |
| GPM49 | 0.302 | 86.31 | 974.0 | 10.0 | 0.304 | 75.81 |
| GPM44 | 0.269 | 74.65 | 998.0 | 5.0 | 0.330 | 131.33 |
| GPM45 | 0.249 | 44.75 | 1072.0 | 5.0 | 0.299 | 48.52 |
| GPM42 | 0.225 | 45.85 | 1158.0 | 9.0 | 0.274 | 16.76 |
| GPM46 | 0.222 | 22.60 | 1162.0 | 5.0 | 0.237 | 8.63 |
| GPM50 | 0.102 | 0.57 | 1240.0 | 10.0 | 0.011 | 0.44 |
| GPM48 | 0.0062 | $7.7 \times 10^{-5}$ | 1259.0 | 10.0 | 0.016 | 1.29 |
| GPM47 | 0.0096 | $3.8 \times 10^{-4}$ | 1260.0 | 5.0 | 0.017 | 1.49 |
| **A-series** | | | | | | |
| GPM35 | 0.376 | 810.25 | 872.0 | 10.0 | 0.370 | 267.46 |
| GPM36 | 0.305 | 198.54 | 982.0 | 10.0 | 0.340 | 238.58 |
| GPM39 | 0.206 | 17.64 | 1073.0 | 10.0 | 0.220 | 26.04 |
| GPM33† | 0.0283 | 0.0473 | 1258.0 | 7.5 | 0.040 | 0.04 |
| **SR150-series** | | | | | | |
| GPM34 | 0.360 | 431.69 | 848.0 | 10.5 | 0.365 | 300.84 |
| GPM12 | 0.340 | 281.88 | 880.0 | 10.4 | 0.370 | 472.05 |
| GPM37 | 0.383 | 773.93 | 973.0 | 10.0 | 0.350 | 230.12 |
| GPM19† | 0.290 | 105.54 | 1072.0 | 7.7 | 0.291 | 147.61 |
| GPM40 | 0.174 | 14.32 | 1074.0 | 10.0 | 0.208 | 28.21 |
| GPM30 | 0.262 | 72.66 | 1087.0 | 7.5 | 0.297 | 162.72 |
| GPM17 | 0.214 | 23.53 | 1185.0 | 9.2 | 0.199 | 17.96 |
| GPM31 | 0.0184 | 0.0319 | 1253.0 | 5.0 | 0.023 | 0.01 |

† *Sample scanned with the micro-CT scanner as well.*